

AnyNav: Visual Neuro-Symbolic Friction Learning for Off-road Navigation

Taimeng Fu¹, Zitong Zhan¹, Zhipeng Zhao¹, Shaoshu Su¹, Xiao Lin¹, Ehsan Tarkesh Esfahani¹, Karthik Dantu¹, Souma Chowdhury¹, and Chen Wang¹

Abstract

Off-road navigation is essential for a wide range of applications in field robotics such as planetary exploration and disaster response. However, it remains an unresolved challenge due to the unstructured environments and inherent complexity of terrain-vehicle interactions. Traditional physics-based methods struggle to accurately model the nonlinear dynamics of these interactions, while data-driven approaches often suffer from overfitting to specific motion patterns, vehicle sizes, and types, limiting their generalizability. To overcome these challenges, we introduce a vision-based friction estimation framework grounded in neuro-symbolic principles, integrating neural networks for visual perception with symbolic reasoning for physical modeling. This enables significantly improved generalization abilities through explicit physical reasoning incorporating the predicted friction. Additionally, we develop a physics-informed planner that leverages the learned friction coefficient to generate physically feasible and efficient paths, along with corresponding speed profiles. We refer to our approach as AnyNav and evaluate it in both simulation and real-world experiments, demonstrating its utility and robustness across various off-road scenarios and multiple types of four-wheeled vehicles. These results mark an important step toward developing neuro-symbolic spatial intelligence to reason about complex, unstructured environments and enable autonomous off-road navigation in challenging scenarios. Video demonstrations are available at <https://sairlab.org/anynav/>, where the source code will also be released.

Keywords

Off-road Navigation, Vehicle-terrain Interaction, Friction, Neuro-symbolic Learning, Visual Planning

1 Introduction

Off-road navigation is crucial for autonomous systems to operate in unstructured and unpredictable environments without traditional road networks (Di and Shi 2021). It is vital for various robotic applications such as planetary exploration (Wang et al. 2024b), disaster response (Schwarz et al. 2017), and agricultural automation (Zhang et al. 2024).

Unlike structured on-road environments, off-road terrains exhibit diverse and irregular features such as loose gravel, mud, sand, and vegetation, each affecting vehicle dynamics differently (Islam et al. 2022). These terrains introduce complicated nonlinear interactions between the vehicle’s wheels and the terrain. Despite numerous efforts, accurately predicting vehicle-terrain interactions while ensuring generalizability across different terrain types and vehicle configurations remains an open challenge.

Physics-based methods (Tanelli et al. 2012; Zhu et al. 2016) were developed to explicitly model the fundamental laws governing vehicle-terrain interactions. However, they cannot capture the complexities and variability of natural environments. Later, machine learning techniques have shown promise in end-to-end vehicle control by learning the dynamics model from large datasets (Wang et al. 2022, 2024c). However, they often struggle with overfitting to specific motion patterns and vehicle platforms, as their training processes tightly couple terrain properties with robot configurations. Triest et al. (2022) directly learns the dynamics of a specific vehicle from historical dynamic data collected from the same vehicle. However, when the

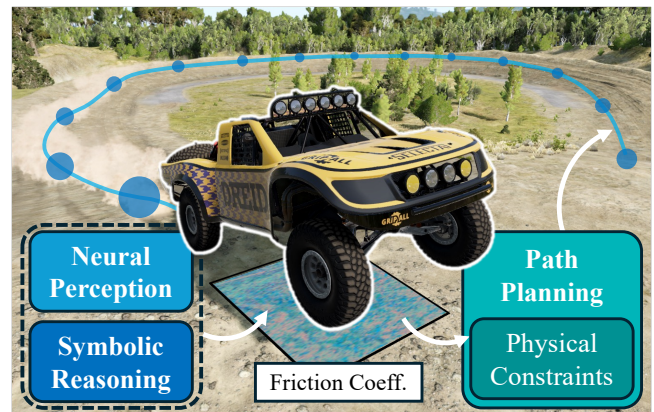


Figure 1. We tackle the challenges of off-road navigation by developing AnyNav, a neuro-symbolic framework for predicting friction coefficient and integrating these predictions as physical constraints in path planning for reliable navigation.

terrain or vehicle type changes, the learned dynamics become inapplicable, limiting its generalizability. Furthermore, their reasoning processes operate as black boxes, introducing risks for system behavior in safety-critical tasks.

¹University at Buffalo, NY 14260, USA

Corresponding author:

Chen Wang, Spatial AI & Robotics (SAIR) Lab, Department of Computer Science and Engineering, University at Buffalo, NY 14260, USA.

Recent advancements in neuro-symbolic learning aim to address the limitations of data-driven methods by combining symbolic reasoning with neural perception (Wu 2024). This hybrid approach enables the integration of expert knowledge, such as physical laws, into the learning process, improving the system’s interpretability. For example, Greydanus et al. (2019) and Saemundsson et al. (2020) demonstrated the feasibility of neuro-symbolic approaches in modeling simple physical processes, such as pendulums and mass-spring systems. However, their performance depends on well-distributed noiseless data from simulations, making them unsuitable for reasoning about highly complex off-road navigation. Similarly, PhysORD (Zhao et al. 2024) applied neuro-symbolic learning for trajectory prediction; however, its learned dynamics model remains specific to a particular vehicle, limiting its generalizability.

Achieving generalizable and interpretable off-road navigation is a complex task requiring a deep understanding of vehicle dynamics. A crucial factor is the friction coefficient, which plays a vital role in predicting how a vehicle will behave in various terrain conditions. To address this challenge, we propose a framework, AnyNav, leveraging the friction coefficient as an intermediary variable to decouple off-road navigation into two distinct modules: neuro-symbolic friction learning and physics-infused path planning. As shown in Figure 1, both modules are grounded in a unified set of physical principles, ensuring interpretability and generalizability across diverse vehicles and terrains.

Previous friction prediction works either require a tactile sensor to touch the object of interest (Ewen et al. 2024) or segment terrain regions to assign predefined parameters (Brandao et al. 2016). In contrast, our neural module estimates friction coefficients directly from visual inputs. Additionally, we employ a symbolic physical reasoning engine to infer the expected vehicle dynamics based on the predicted friction coefficients and supervise the neural module to align the inferred and observed dynamics. This approach eliminates the reliance on ground truth labels, ensuring strong adaptability to diverse terrain conditions. To incorporate the learned friction into a navigation system, we developed a physics-infused planner that leverages friction properties, terrain geometry, and vehicle capabilities to generate paths and speed profiles. This ensures that the planning results comply with physical laws, avoiding implausible scenarios such as climbing a hill with insufficient friction or driving at high speeds in bumpy regions. In summary, our contributions include:

- We propose AnyNav, a neuro-symbolic framework for friction learning with physics-infused path planning, offering interpretability and achieving higher generalizability in complex and unstructured environments.
- The neuro-symbolic module estimates friction coefficients from visual inputs across diverse off-road terrains. It is supervised through aligning symbolically inferred and observed vehicle dynamics.
- The physics-infused planner generates paths and speed profiles while adhering to physical constraints, considering factors such as terrain friction, elevation, roughness, route distance, and vehicle speed.
- Experiments in both simulation and real world demonstrate the robustness and reliability of our

navigation system across various off-road scenarios and multiple vehicle types.

2 Related Works

2.1 Physics-based Methods

Physics-based approaches have been widely used for modeling vehicle dynamics in both structured and unstructured environments, by explicitly incorporating fundamental physical principles (Di and Shi 2021). The kinematic bicycle model (Ailon et al. 2005; Polack et al. 2018) leverages Newtonian mechanics to predict vehicle state transitions effectively in controlled scenarios. Enhancements like the Kalman Filter (Reina and Messina 2019) and Monte Carlo simulations (Wu et al. 2015) introduce stochastic elements to manage uncertainties, particularly in off-road conditions. However, these models often rely on idealized assumptions and simplified dynamics, which limit their applicability in complex, highly non-linear terrains.

A parallel line of research focuses on modeling tire-terrain interactions (Taheri et al. 2015). These methods often employ principles of soil mechanics and accounting for tire deformation, as demonstrated by Madsen et al. (2012); Wasfy et al. (2018); Serban et al. (2017). While effective under certain conditions, these models typically depend on predefined parameters, reducing their adaptability to dynamic and heterogeneous environments. Tanelli et al. (2012) integrated empirical observations with theoretical frameworks to estimate certain parameters, but their approach was limited to straight-line driving.

2.2 Data-driven Approaches

To address the limitations of physics-based methods, data-driven approaches for terrain analysis have gained significant attention. For instance, Vulpi et al. (2021); Ewen et al. (2022) employed neural networks to predict terrain properties through visual segmentation. Wellhausen et al. (2019); Castro et al. (2023) estimated terrain traversability using motion data derived from torque sensors or IMU measurements. These methods exhibit notable advancements in capturing the variability and complexity inherent in unstructured off-road environments.

In addition to terrain analysis, machine learning techniques have been applied to predicting robot dynamics. Tremblay et al. (2021); Wang et al. (2023b); Narayanan et al. (2020) utilized neural networks to effectively capture sequential dependencies, delivering robust status and trajectory predictions over extended time horizons. Xiao et al. (2024) developed a transformer-based vehicle dynamics model using extensive training data from multiple simulators. However, these data-driven approaches face challenges in generalization, largely due to their dependence on extensive labeled datasets and the absence of explicit physical reasoning. Efforts such as TartanDrive (Triest et al. 2022) have established benchmarks for off-road datasets with diverse terrains but remain overfitted to specific vehicles.

2.3 Physics-Infused Networks

The fusion of physics-based insights with neural networks has emerged as a promising direction for modeling dynamic systems. Approaches such as Neural Ordinary Differential

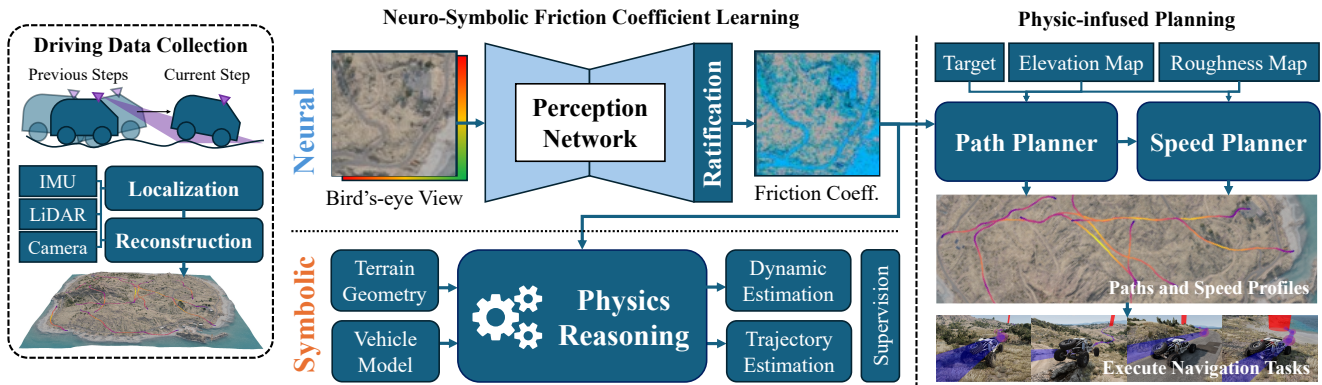


Figure 2. The AnyNav framework comprises a neuro-symbolic module and a planning module. The neuro-symbolic module has a neural network to predict friction coefficients from visual inputs, guided by symbolic physics reasoning for supervision. The planning module leverages friction knowledge to determine physically feasible and efficient paths and speeds for off-road navigation.

Equations (Chen et al. 2018) and Hamiltonian Neural Networks (Greydanus et al. 2019) embed conservation laws and system dynamics into learning processes, preserving the structure of physical systems. Variational Integrator Networks (Saemundsson et al. 2020) and their extensions (Havens and Chowdhary 2021; Duruisseaux et al. 2023) have shown promise in imposing geometric and physical constraints, such as symmetries. These methods have demonstrated accuracy in modeling simple physics, such as pendulums and mass-spring systems. However, real-world applications remain challenging due to the increased complexity and uncertainty inherent in practical environments, as highlighted by Zhao et al. (2024).

Recent advancements in physics-infused learning have demonstrated significant potential in addressing such challenges, particularly in off-road applications. Frey et al. (2024) proposed a self-supervised framework that trains a traversability prediction network using pseudo-labels generated by X-Racer, a physics-based off-road autonomy stack. Zhao et al. (2024) integrated learnable components into the vehicle’s Lagrangian equations, constraining the learning process with physics principles such as energy conservation. Agishev et al. (2023) predicted terrain height and stiffness properties from visual inputs, integrating the calculated supporting force through a differentiable physics engine for supervision. Chen et al. (2024) introduced a network for estimating friction and stiffness from proprioceptive observations, initially trained in simulation and later adapted to real-world environments. Cai et al. (2024) introduced physics priors into evidential neural networks, incorporating physics knowledge into the learning process via an uncertainty-aware loss function. However, accurately predicting the friction coefficient of diverse off-road terrains and leveraging this knowledge for reliable long-term navigation remains a challenging open problem.

3 Neuro-Symbolic Friction Learning

Overview The proposed AnyNav framework is illustrated in Figure 2, which consists of two main modules: a neuro-symbolic module for friction coefficient estimation (Section 3), and a physics-infused planning module for off-road navigation (Section 4). In the neuro-symbolic

module, a neural network takes the terrain bird’s eye view (BEV) images as input and estimates pixel-wise friction coefficients, while a symbolic reasoning engine utilizes these estimations to simulate the vehicle’s dynamics to provide supervision signals. In the planning module, a path planner and a speed planner generate safe and efficient paths and speed profiles, taking into account physical constraints such as terrain friction, elevation changes, ground roughness, route distance, and vehicle capabilities. This architecture decomposed the terrain-specific physics modeling from vehicle-related navigation tasks, ensuring improved generalizability. The two modules are connected through interpretable, universal physics principles, achieving excellent generalizability across different vehicles and exceptional robustness in unfamiliar terrains.

3.1 Neural Perception Module

Our neural perception module aims to estimate key parameters in the friction model from visual inputs. Different terrain types, such as asphalt and grass, or the same type under varying conditions, like dirt and mud, typically exhibit distinct visual appearances and friction coefficients. The neural network learns the relationship between a terrain’s appearance and its corresponding friction coefficient. In contrast to previous works (Vulpi et al. 2021; Ewen et al. 2022) that categorize the environment into predefined types, our approach involves regressing the parameters in the friction model. This is because the real world presents an infinite variety of conditions (e.g., *muddy grass*, *sandy dirt*), each with nuanced frictional properties. By regressing the friction model parameters, our approach enables the model to generalize beyond a fixed set of predefined classes, allowing for more effective adaptation to diverse conditions.

3.1.1 Stribeck Friction Model We use the Stribeck Model (Armstrong and de Wit 1995) to define friction, which describes the relationship between friction coefficient and the wheel skidding velocity when losing traction on the ground, capturing the transition from static to kinetic friction. It accurately represents real-world frictional behaviors, incorporating both the Stribeck and viscous effects, making it particularly suitable for modeling conditions with various tire slip speeds. Denote the wheel skidding speed, measured

by the relative speed between the tire and ground, as v_{rel} . The friction coefficient μ can be computed as

$$\begin{aligned} \mu &= \text{Stribeck}(v_{rel}; \mu_s, \mu_d, v_S, \mu_v) \\ &= \sqrt{2}e^{(\mu_s - \mu_d)} \exp\left(-\left(\frac{v_{rel}}{v_S}\right)^2\right) \frac{v_{rel}}{v_S} \\ &\quad + \mu_d \tanh\left(\frac{10\sqrt{2}v_{rel}}{v_S}\right) + \mu_v v_{rel}, \end{aligned} \quad (1)$$

where v_S is the Stribeck velocity and μ_s , μ_d , and μ_v represent the static, dynamic, and viscous coefficients, respectively. Each terrain type typically has unique values for these parameters. Specifically, μ_s represents the friction coefficient before the wheel begins to slide and is typically higher than μ_d , the coefficient during sliding. The parameter v_S defines the threshold sliding speed marking the transition from static to dynamic friction, while μ_v characterizes the fluid resistance experienced by the wheel. We denote the set of Stribeck coefficients as $\mathbf{S} = \{\mu_s, \mu_d, v_S, \mu_v\}$. An example illustrating learned friction curves can be found in Figure 10.

3.1.2 Neural Network We adopt a simple UNet (Ronneberger et al. 2015) to predict pixel-wise Stribeck friction coefficients and denote it as \mathbf{S}_{pred} . The model takes a terrain image patch centered on each wheel’s contact point as input $\mathbf{X}_{in} \in \mathbf{R}^{4 \times H \times W}$, which is a four-channel (three color and one height channel) BEV map. This BEV map is obtained by running a dense simultaneous localization and mapping algorithm (SLAM) using past visual and LiDAR observations.

The network is applied individually to each wheel, accommodating potential variations in terrain across wheels. The model weights are shared among wheels under the assumption that they are identical in structure and function. These shared model weights also ensure that the model learns general physical principles that apply to all wheels.

3.2 Symbolic Reasoning Module

The symbolic reasoning module estimates the vehicle’s dynamics at each step based on the predicted friction coefficients, terrain geometry, and vehicle model. We first show the vehicle’s modeling in Section 3.2.1, calculate the normal force on each wheel in Section 3.2.2, estimate the friction force in Section 3.2.3, and integrate these dynamics over time to generate the trajectory in Section 3.2.4.

3.2.1 Vehicle Model We model the vehicle as a rigid body fixed in a local coordinate frame, \mathcal{V} . Here we only study four-wheeled vehicles. It consists of a set of N_m mass points, $(\mathbf{pt}_i^{\mathcal{V}}, \text{mass}_i)$ for $i = 1, \dots, N_m$, where $\mathbf{pt}_i^{\mathcal{V}} \in \mathbf{R}^3$ represents the position in \mathcal{V} , and $\text{mass}_i \in \mathbf{R}^+$ is the mass of that point. An exemplar distribution of a vehicle’s mass points is illustrated as blue dots in Figure 3. This flexible structure allows for the modeling of any vehicle’s geometry and mass distribution. The total mass of the vehicle is

$$M = \sum_{i=1}^{N_m} \text{mass}_i, \quad (2)$$

and the center of mass (COM) in \mathcal{V} is given by

$$\mathbf{pt}_{\text{COM}}^{\mathcal{V}} = \frac{\sum_{i=1}^{N_m} \text{mass}_i \cdot \mathbf{pt}_i^{\mathcal{V}}}{M}. \quad (3)$$

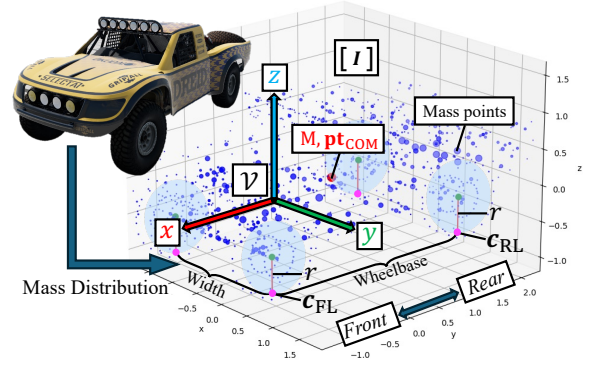


Figure 3. The configurable vehicle model. The blue dots represent the mass distribution, with their size proportional to the magnitude of the mass at each point. M is the total mass, \mathbf{pt}_{COM} is the center of mass, \mathbf{I} is the rotational inertia matrix, \mathbf{c} are wheel contact points, and r is wheel radius.

Define the position relative to COM as $\delta_i = \mathbf{pt}_i^{\mathcal{V}} - \mathbf{pt}_{\text{COM}}^{\mathcal{V}}$, the rotational inertia matrix around COM is computed as

$$\mathbf{I}^{\mathcal{V}} = \sum_{i=1}^{N_m} \text{mass}_i \left(\|\delta_i\|^2 \mathbf{I}_{3 \times 3} - \delta_i \delta_i^T \right). \quad (4)$$

We define the world coordinate frame, \mathcal{W} , in which the vehicle pose is represented as $\xi = [\mathbf{t} \ \mathbf{q}] \in SE(3)$, where $\mathbf{t} \in \mathbf{R}^3$ is the translation vector, $\mathbf{q} \in SO(3)$ is the rotation quaternion. When in motion, the vehicle has a velocity $\mathbf{v} \in \mathbf{R}^3$ and an angular velocity $\boldsymbol{\omega} \in \mathbf{R}^3$, both expressed in \mathcal{W} . Furthermore, we denote the linear acceleration as $\mathbf{a} \in \mathbf{R}^3$ and the angular acceleration as $\boldsymbol{\alpha} \in \mathbf{R}^3$. For generalizability, we also model the geometrical size of the vehicle. Denote the ground contact point of the front-left, front-right, rear-left, and rear-right wheels as $\mathbf{c}_w^{\mathcal{V}} \in \mathbf{R}^3$ for $w \in \{\text{FL}, \text{FR}, \text{RL}, \text{RR}\}$, and the wheel radius as $r \in \mathbf{R}^+$, the wheelbase and width can be easily computed from these contact points. Figure 3 illustrates an exemplar vehicle model.

3.2.2 Weight Transfer When a vehicle contacts the ground, the ground exerts a supportive force on its wheels, known as the normal force. However, this force is not evenly distributed across all four wheels because its allocation is affected by weight transfer during acceleration (Su et al. 2023). Accurately estimating the normal force on each wheel is essential for determining the corresponding friction force.

To analyze the effect of weight transfer, we utilize the bicycle model (Ailon et al. 2005) and examine it along both the longitudinal and transverse axes. For the sake of simplicity, we explain the analysis along the longitudinal axis, as the principles could be applied similarly along the transverse axis. As shown in Figure 4, consider the vehicle is accelerating at a rate a on an upward slope inclined at an angle θ . The gravitational force Mg acts on the COM, which is elevated above the slope by a height h . The front and rear wheels’ contact points are referred to as \mathbf{c}_f and \mathbf{c}_r corresponding to the exerted front normal force F_N^{front} and rear normal force F_N^{rear} , respectively. The distance along the slope from the COM to the front and rear contact points are denoted as d_f and d_r , respectively. To analyze the system, we take \mathbf{c}_r as the reference point and establish a 2D local frame at this contact point, where the two axes are parallel and perpendicular to the slope, respectively. In this non-inertial

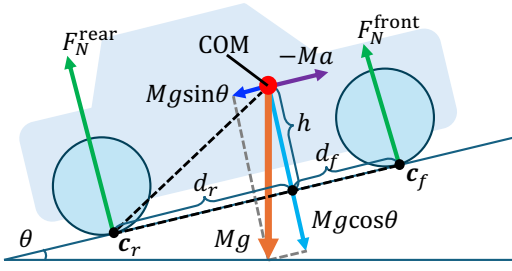


Figure 4. Analysis of weight transfer of a vehicle on an inclined plane. The vehicle accelerates down an incline at an angle θ . The gravitational force Mg acts on the COM, located at a height h above the slope. The normal forces at the front and rear wheels, F_N^{front} and F_N^{rear} , act at contact points \mathbf{c}_f and \mathbf{c}_r , respectively. The distances along the slope from the COM to these contact points are denoted as d_f and d_r . The inertial force from the vehicle's acceleration, $-Ma$, and the components of gravitational force, $Mg \sin \theta$ and $Mg \cos \theta$, are also shown for analysis of weight transfer.

frame, an equivalent inertial force $-Ma$ acts on the COM due to acceleration. Applying the conservation of angular momentum w.r.t. \mathbf{c}_r gives us

$$(d_r + d_f)F_N^{\text{front}} + hMg \sin \theta + hMa - d_rMg \cos \theta = 0, \quad (5)$$

where the frictional forces are excluded, as they have zero moment arms relative to \mathbf{c}_r . Solving for F_N^{front} , we obtain

$$F_N^{\text{front}} = \frac{-hMg \sin \theta - hMa + d_rMg \cos \theta}{d_r + d_f}. \quad (6)$$

Similarly, F_N^{rear} can be obtained by performing an analysis at \mathbf{c}_f , hence the ratio of the front-to-rear normal force is

$$\beta := \frac{F_N^{\text{front}}}{F_N^{\text{rear}}} = \frac{hMg \sin \theta + hMa + d_fMg \cos \theta}{-hMg \sin \theta - hMa + d_rMg \cos \theta}. \quad (7)$$

A similar process can be applied to compute the transverse force ratio $\gamma := F_N^{\text{left}} / F_N^{\text{right}}$. Therefore, the magnitudes of the individual normal forces at the four wheels are

$$\begin{aligned} F_N^{\text{FL}} &= \frac{\beta}{1 + \beta} \cdot \frac{\gamma}{1 + \gamma} \cdot Mg \cos \theta, \\ F_N^{\text{FR}} &= \frac{\beta}{1 + \beta} \cdot \frac{1}{1 + \gamma} \cdot Mg \cos \theta, \\ F_N^{\text{RL}} &= \frac{1}{1 + \beta} \cdot \frac{\gamma}{1 + \gamma} \cdot Mg \cos \theta, \\ F_N^{\text{RR}} &= \frac{1}{1 + \beta} \cdot \frac{1}{1 + \gamma} \cdot Mg \cos \theta. \end{aligned} \quad (8)$$

Finally, the normal force vectors \mathbf{F}_N^w can be obtained by multiplying the magnitudes computed in (8) by a unit normal vector pointing in the direction perpendicular to the slope.

3.2.3 Friction Force The friction force depends on the predicted friction coefficients \mathbf{S}_{pred} and the skidding speed of the wheel $\mathbf{v}_{\text{rel}}^w$. The skidding speed is non-zero if the wheel is losing traction on the ground. It is measured by the difference between the linear velocity of the wheel's center and its edge,

$$\mathbf{v}_{\text{rel}}^w = \mathbf{v}_e^w - \mathbf{v}_c^w. \quad (9)$$

The linear velocity of a wheel center \mathbf{v}_c^w is determined by combining the vehicle body's velocity with a tangent velocity

resulting from the vehicle's rotation,

$$\mathbf{v}_c^w = \mathbf{v} + \boldsymbol{\omega} \times (\mathbf{c}_w - \mathbf{p}_{\text{COM}}), \quad (10)$$

where \times denotes the cross product between vectors. The linear velocity on the edge of a wheel is computed from its RPM measurement,

$$\mathbf{v}_e^w = 2\pi r \cdot \frac{\text{RPM}^w}{60} \cdot \mathbf{d}^w, \quad (11)$$

where \mathbf{d}^w is the unit direction vector of wheel w . Lastly, we sample the Stribeck curve at the calculated skidding speed $\mathbf{v}_{\text{rel}}^w$ to determine the friction coefficient of each wheel,

$$\mu^w = \text{Stribeck}(\|\mathbf{v}_{\text{rel}}^w\|; \mathbf{S}_{\text{pred}}). \quad (12)$$

Combining with the estimated normal force in Section 3.2.2 allows us to calculate the friction force exerted on a wheel w

$$\mathbf{F}_f^w = -\mu^w \|\mathbf{F}_N^w\| \cdot \frac{\mathbf{v}_{\text{rel}}^w}{\|\mathbf{v}_{\text{rel}}^w\|}, \quad (13)$$

pointing at the opposite direction of the relative velocity.

3.2.4 Semi-implicit Euler Integrator To predict the trajectory of a vehicle, we utilize the semi-implicit Euler method (Liu et al. 2004). It estimates the vehicle's motion considering its pose $\boldsymbol{\xi} = [\mathbf{t} \ \mathbf{q}]$, linear velocity \mathbf{v} , and angular velocity $\boldsymbol{\omega}$, from an initial state $\{\boldsymbol{\xi}_0, \mathbf{v}_0, \boldsymbol{\omega}_0\}$ using the vehicle's acceleration. The total external force is

$$\mathbf{F} = Mg + \sum_w (\mathbf{F}_N^w + \mathbf{F}_f^w), \quad (14)$$

and the total torque on the COM is

$$\boldsymbol{\tau} = \sum_w (\mathbf{c}_w - \mathbf{p}_{\text{COM}}) \times (\mathbf{F}_N^w + \mathbf{F}_f^w). \quad (15)$$

The linear and angular accelerations are computed as

$$\mathbf{a} = \frac{d\mathbf{v}}{dt} = \frac{\mathbf{F}}{M}, \quad (16)$$

$$\boldsymbol{\alpha} = \frac{d\boldsymbol{\omega}}{dt} = (\mathbf{I}^w)^{-1} \boldsymbol{\tau}, \quad (17)$$

where \mathbf{I}^w is the rotation inertia matrix in world coordinate,

$$\mathbf{I}^w = \mathbf{q}^{-1} \mathbf{I}^y \mathbf{q}. \quad (18)$$

Finally, we apply the semi-implicit Euler method to integrate the velocity, angular velocity, and pose over a time step Δt ,

$$\mathbf{v}_{\Delta t} = \mathbf{v} + \mathbf{a}\Delta t, \quad (19)$$

$$\boldsymbol{\omega}_{\Delta t} = \boldsymbol{\omega} + \boldsymbol{\alpha}\Delta t, \quad (20)$$

$$\mathbf{t}_{\Delta t} = \mathbf{t} + \mathbf{v}_{\Delta t}\Delta t, \quad (21)$$

$$\mathbf{q}_{\Delta t} = \text{Normalize} \left(\mathbf{q} + \frac{1}{2} ([\boldsymbol{\omega}_{\Delta t}, 0] \mathbf{q}) \Delta t \right), \quad (22)$$

where $[\boldsymbol{\omega}_{\Delta t}, 0]$ is a quaternion with an imaginary part of $\boldsymbol{\omega}_{\Delta t}$ and a real part of 0. $\text{Normalize}(\cdot)$ projects the computed result back to a unit quaternion. By performing the integration iteratively over time, we can estimate the trajectory over N steps, $\{\boldsymbol{\xi}_i^{\text{est}}\}_{i=1}^N$.

3.3 Training Strategies

One of the significant challenges in training a neural module for predicting friction coefficients is generating physically realistic ground truth. This is particularly difficult because the friction coefficient is a hidden variable within the vehicle-terrain system, making it impossible to measure without specialized equipment. However, vehicle dynamics, which are strongly influenced by the friction coefficient,

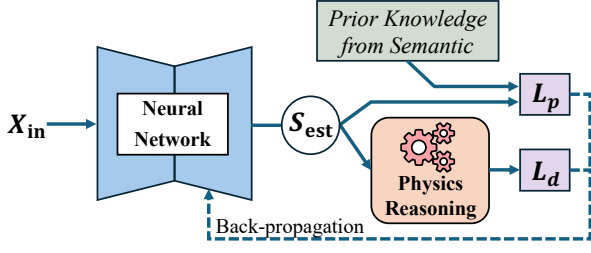


Figure 5. The training strategy in simulation. The input image \mathbf{X}_{in} is passed through a neural network to produce estimations of Stribeck coefficients \mathbf{S}_{est} . These estimations are used in a physics reasoning module to compute the dynamics loss (L_d) by comparing the inferred and ground truth dynamics. Simultaneously, prior semantic knowledge about terrain types supervises the predicted coefficients via the prior knowledge loss (L_p). The neural model is trained with both losses.

can be easily obtained using an IMU. Therefore, we use the symbolic module to reason the effect of the predicted friction coefficients on vehicle dynamics to create a supervision signal for the neural module. To accommodate the differences in data availability and noise levels between virtual and real-world scenarios, we introduce two tailored training strategies for each environment.

3.3.1 Training in Simulation Simulated environments offer a unique advantage for training neural networks from scratch. Unlike the real world, these environments simplify physical effects and provide precise, noiseless sensor measurements, making them ideal for initial training. To leverage this, our neuro-symbolic learning approach combines two distinct loss functions: a dynamics loss and a prior knowledge loss, as illustrated in Figure 5.

The dynamics loss function penalizes the discrepancy between the dynamics estimations consisting of linear and angular accelerations, \mathbf{a}_{est} and $\boldsymbol{\alpha}_{est}$, and the corresponding ground truth, \mathbf{a}_{gt} and $\boldsymbol{\alpha}_{gt}$. This loss is defined as

$$L_d = \text{Huber}(\mathbf{a}_{est}, \mathbf{a}_{gt}) + \text{Huber}(\boldsymbol{\alpha}_{est}, \boldsymbol{\alpha}_{gt}), \quad (23)$$

where $\text{Huber}(\cdot)$ is the Huber loss (Huber 1992). During training, the gradient is back-propagated through the differentiable physical reasoning engine to the neural model.

While the dynamics loss provides indirect supervision on dynamics, the prior knowledge loss based on accurate terrain semantic labels directly supervises the Stribeck coefficients prediction. Specifically, for each terrain type u , we assign a prior $\mathbf{S}_{prior}(u)$ to represent its typical values of Stribeck coefficients. The prior knowledge loss is then defined as

$$L_p = \text{L1Loss}(\mathbf{S}_{pred}, \mathbf{S}_{prior}(u)). \quad (24)$$

The final loss function is a combination of the two,

$$L = L_d + \lambda L_p, \quad (25)$$

where λ is a hyperparameter. This ensures the predicted friction effects align with both the observed dynamics and the typical terrain property.

3.3.2 Fine-tuning in the Real World Training the model in real-world settings presents greater challenges compared to simulation environments. Two major obstacles arise: the unavailability of terrain-type segmentation, which prevents

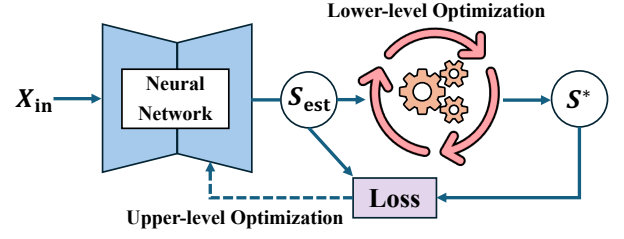


Figure 6. The bilevel optimization framework tackling real-world training challenges with Imperative Learning.

The upper-level optimization uses pseudo-labels derived from the lower-level optimization, which jointly optimize the Stribeck coefficients, the dynamics model, and vehicle parameters. Neural network updates are driven by the refined Stribeck coefficients to improve predictions under real-world conditions with noisy inputs and uncertain parameters.

the application of prior knowledge loss, and the introduction of significant bias in the dynamics loss due to noisy sensor measurements. Additionally, substantial uncertainties exist in the vehicle model, particularly in determining the mass distribution. To address these challenges, we developed a more robust method using bilevel optimization as shown in Figure 6, inspired by the concept of imperative learning (IL) (Wang et al. 2024a). We design a lower-level optimization (26b) to jointly optimize the predicted Stribeck coefficients \mathbf{S}_{pred} and vehicle parameters such that they satisfy a set of physical constraints C . The optimized coefficients \mathbf{S}^* then served as pseudo-labels to update the neural network f_θ in upper-level optimization (26a), where θ is model weights. The process is formulated as

$$\min_{\theta} \|f_\theta(\mathbf{X}_{in}) - \mathbf{S}^*\|_1 \quad (26a)$$

$$\text{s.t. } \mathbf{S}^* = \arg \min_{\mathbf{S}} C(\mathbf{S}_{pred}). \quad (26b)$$

The lower-level optimization operates at each time step $i = 1 \dots N$, where we optimize a set of variables, including the vehicle's poses $\boldsymbol{\xi}_i$, velocities \mathbf{v}_i , rotational inertia $\mathbf{I}^{\mathcal{V}}$, as well as the per-wheel Stribeck coefficients \mathbf{S}_i^w , wheel RPM RPM_i^w , and normal forces $(\mathbf{F}_N^w)_i$. We initialize these variables as follows: the Stribeck coefficients \mathbf{S}_i^w are set to the model's prediction; $\mathbf{I}^{\mathcal{V}}$ is initialized with a rough estimate; RPM_i^w is initialized based on its measurement; $\boldsymbol{\xi}_i$, \mathbf{v}_i , and $(\mathbf{F}_N^w)_i$ are estimated through propagating the symbolic reasoning module. We optimize these parameters with a set of constraints:

Dynamics Constraints ensure the acceleration estimated by the physical reasoning to align with the IMU measurements,

$$\mathbf{C}_a^{(i)} = \mathbf{a}_{est}^{(i)} - \mathbf{q}_i \mathbf{a}_{IMU}^{(i)}, \quad (27)$$

$$\mathbf{C}_\alpha^{(i)} = \boldsymbol{\alpha}_{est}^{(i)} - \mathbf{q}_i \boldsymbol{\alpha}_{IMU}^{(i)}. \quad (28)$$

Integration Constraints ensure the rotation and velocity are consistent with integrated IMU sensing over time i to $i+1$,

$$\mathbf{C}_v^{(i)} = (\mathbf{v}_{i+1} - \mathbf{v}_i) - \mathbf{q}_i \mathbf{a}_{IMU}^{(i)} \Delta t, \quad (29)$$

$$(\mathbf{C}_q)_i = \text{Log} \left(\mathbf{q}_{i+1}^{-1} \left(\mathbf{q}_i + \frac{1}{2} \left([\boldsymbol{\omega}_{IMU}^{(i)}, 0] \mathbf{q}_i \right) \Delta t \right) \right), \quad (30)$$

where $\text{Log}(\cdot)$ is the Log mapping to Lie algebra.

Stribeck Constraint ensures that the Stribeck coefficients remain within reasonable ranges and avoid rapid fluctuations,

thereby promoting temporal consistency,

$$C_s^{(i)} = \max\left(0, \frac{S_i^w}{S_{max}} - 1\right)^2 + (S_{i+1}^w - S_i^w), \quad (31)$$

where $S_{max} \in \mathbb{R}^4$ is the upper-bound value for each channel of the Stribeck coefficients.

Wheel Speed Constraint ensures that the wheel RPM parameter remains close to its measurement,

$$C_w^{(i)} = \text{RPM}_i^w - (\text{RPM}_{meas})_i^w. \quad (32)$$

The objective of lower-level optimization is the weighted sum of all these constraints across all time steps,

$$C = \sum_{i=1}^{N-1} \left(C_a^{(i)T} \mathbf{W}_a C_a^{(i)} + C_\alpha^{(i)T} \mathbf{W}_\alpha C_\alpha^{(i)} + C_v^{(i)T} \mathbf{W}_v C_v^{(i)} \right. \\ \left. + C_q^{(i)T} \mathbf{W}_q C_q^{(i)} + C_s^{(i)T} \mathbf{W}_s C_s^{(i)} + C_w^{(i)T} \mathbf{W}_w C_w^{(i)} \right), \quad (33)$$

where \mathbf{W}_\cdot are diagonal weighting matrices used to balance each term. We employ the 2nd-order Levenberg-Marquardt (LM) algorithm in PyPose (Wang et al. 2023a) to solve it, and use the optimized Stribeck coefficient as pseudo-labels to fine-tune the neural model.

4 Physics-Infused Planning

Building on the predicted friction, we can now integrate this knowledge into a physics-infused planning system. By understanding this important terrain property, the planner can make informed decisions about both route selection and speed planning, taking into account the physical interactions between the vehicle and its environment. For example, a “smart” planner may prefer high-friction areas to facilitate hill climbing and slow down when navigating low-friction areas to ensure stable steering. This approach enables more adaptive and responsive route and speed planning, tailored to specific terrain conditions. Additionally, as an interpretable white-box system, it offers generalizability across diverse environments, with predictable and deterministic behavior that enhances reliability in real-world applications. We next present the design of this physics-infused planning system, including the map structure in Section 4.1, the path planner in Section 4.2, and the speed planner in Section 4.3.

4.1 Map Structure

The map used is a 2.5D $W \times H$ grid map, consisting of three distinct layers: the Stribeck coefficient layer $\mathbf{SL} \in \mathbb{R}^{W \times H \times 4}$, the elevation layer $\mathbf{EL} \in \mathbb{R}^{W \times H}$, and the roughness layer $\mathbf{RL} \in \mathbb{R}^{W \times H}$. The Stribeck layer is constructed by concatenating patches predicted by the neural model f_θ :

$$\mathbf{SL}_{xy} = f_\theta(\mathbf{X}_{xy}^{\text{in}}), \quad (34)$$

where xy represents the location within the grid and $\mathbf{X}_{xy}^{\text{in}}$ denotes its corresponding input patch. The elevation layer is obtained by averaging the z -coordinates of the reconstructed points within each grid cell,

$$\mathbf{EL}_{xy} = \text{Mean}_{\mathbf{p} \in \text{grid}_{xy}}(z_p). \quad (35)$$

The roughness \mathbf{RL}_{xy} is quantified as the local height variance within each grid cell. For example, bushy and rocky areas have higher roughness values, while paved roads have lower values. To compute roughness, we first fit a plane to all the points \mathbf{p} within each grid cell xy , then calculate the sum of

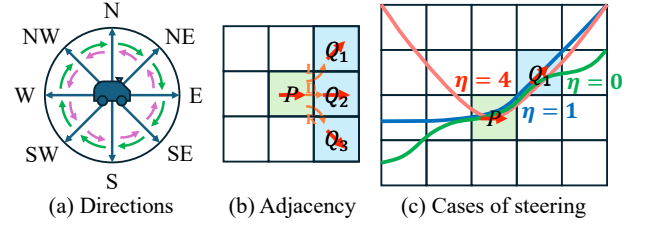


Figure 7. Illustration of vehicle motions and cost components in path planning. (a) The eight possible orientations of the vehicle, with green and purple arrows showing allowable turns based on each step. (b) Example of vertex connections in the graph, where grid cell P with an east-facing orientation connects to neighboring vertices Q_1 , Q_2 , and Q_3 based on permissible motions and steering angles. (c) Depiction of steering cost factor η , varying based on consecutive turns, as illustrated for P and Q_1 transitions; higher penalties are assigned for sharp or consecutive turns in the same direction.

squared distances from each point to the plane,

$$\mathbf{RL}_{xy} = \min_{a,b,d} \sum_{\mathbf{p} \in \text{grid}_{xy}} \left(\frac{|ax_p + by_p - z_p + d|}{\sqrt{a^2 + b^2 + 1}} \right)^2, \quad (36)$$

where the plane is parametrized by $ax + by - z + d = 0$ and can be solved as a nonlinear least square problem.

4.2 Path Planner

We utilize the A* algorithm (Hart et al. 1968) to determine the single-source lowest-cost path. Our cost function incorporates both terrain properties and vehicle steering dynamics for a comprehensive evaluation of route efficiency. To effectively capture the vehicle’s motion and steering in planning, we represent each vertex in the graph as a vehicle state denoted by a 4-tuple of attributes: (x, y, o, m) , where x, y represent the location within the grid, o denotes the eight possible directions of vehicle facing shown in Figure 7(a), and m represents the motion (L : turned left, D : went straight, R : turned right) the vehicle performed in the previous step.

Formally, the shortest path algorithm operates on a graph $\mathbf{G} = (\mathbf{V}, \mathbf{E})$, where each vertex in \mathbf{V} corresponds to a unique combination of (x, y, o, m) . Each vertex P is connected to its neighboring vertices Q_i via edges $(P, Q_i) \in \mathbf{E}$, with the adjacency defined based on the three actions (L, D and R) the vehicles can take at the current state. For example, $P = \{x, y, E, \cdot\}$ has edges to $Q_1 = \{x + 1, y + 1, NE, L\}$, $Q_2 = \{x + 1, y, E, D\}$, and $Q_3 = \{x + 1, y - 1, SE, R\}$, as shown in Figure 7(b). Each edge has an associated cost representing the traversal effort. This cost is composed of the following: **Distance Cost** measures the 2D distance D_d from P to Q . It equals to either 1 or $\sqrt{2}$, depending on whether the vehicle’s movement is horizontal, vertical, or diagonal.

Friction Cost evaluates the combined effects of friction level and viscous strength between P and Q :

$$D_f = \frac{1}{\mu_{PQ}} + \lambda_v \mu_v^{PQ}, \quad (37)$$

where μ_{PQ} is the average friction coefficient under a certain skidding speed v_{rel} .

$$\mu_{PQ} = \text{Stribeck} \left(v_{rel}; \frac{\mathbf{SL}_P + \mathbf{SL}_Q}{2} \right). \quad (38)$$

This skidding speed is a hyperparameter that defines the desired aggressiveness of driving. μ_v^{PQ} is the average viscous coefficient $\mu_v^{PQ} = (\mu_v^P + \mu_v^Q)/2$. λ_v is a hyperparameter.

Slope Cost evaluates how well the vehicle can control its motion on a slope. It is jointly affected by the friction coefficient μ_{PQ} , the slope along line PQ , δ_{PQ} , and the slope perpendicular to line PQ , δ_{\perp} :

$$D_s = \exp\left(\lambda_s \frac{\delta_{PQ}}{\mu_{PQ}}\right) + \exp\left(\lambda_s \frac{\delta_{\perp}}{\mu_{PQ}}\right). \quad (39)$$

We use the exp function to introduce non-linearity; the penalty remains low when friction is sufficient for safe traversal on the slope but increases exponentially beyond a certain threshold. The slopes δ_{PQ} and δ_{\perp} are obtained from the elevation layer **EL**. λ_s is a hyperparameter.

Roughness Cost penalizes the vehicle from traversing on high-roughness regions, which tend to be bumpy and potentially hazardous. To discourage this, we set a roughness threshold σ_{th} , above which the vehicle should avoid traveling. The roughness cost is a piecewise function,

$$D_R = \begin{cases} (\mathbf{RL}_P + \mathbf{RL}_Q)/2 & \text{if } \mathbf{RL}_P < \sigma_{th} \text{ and } \mathbf{RL}_Q < \sigma_{th}, \\ \infty & \text{otherwise.} \end{cases} \quad (40)$$

The above costs account for the terrain properties around the vehicle's position but do not consider whether the vehicle needs to make a turn to reach that position. As a result, the solely relying on these costs could result in twisty paths, which are unfavorable for high-speed driving. Therefore, we introduced an additional steering cost to penalize unnecessary turns.

Steering Cost is applied when a turn occurs, encouraging path straightness whenever feasible. It is inversely proportional to the friction coefficient μ_{PQ} , scaled by a factor η ,

$$D_t = \begin{cases} \frac{\eta}{\mu_{PQ}} & \text{if } o_P \neq o_Q, \\ 0 & \text{otherwise,} \end{cases} \quad (41)$$

where

$$\eta = \begin{cases} 4 & \text{if } m_P = m_Q = L \text{ or } m_P = m_Q = R, \\ 1 & \text{if } m_P = D \text{ and } m_Q \neq D, \\ 0 & \text{if } m_P = L, m_Q = R \text{ or } m_P = R, m_Q = L. \end{cases} \quad (42)$$

When there are two consecutive turns in the same direction, we set η a larger value to further penalize the large angle steering; when there are two consecutive turns in opposite directions, we set $\eta = 0$ since this closely approximates a straight line after smoothing. Figure 7(c) illustrates these steering patterns and the effect of η .

With these physics-infused costs defining the traversability between adjacent grids, we use the A* algorithm to find the most traversable path. The heuristic function is defined as the Euclidean distance from the current grid to the target grid, which is both admissible and consistent. After searching the shortest path, we fit a spline to the path to smooth the resulting trajectory. The smoothed path is denoted as a list of checkpoints $\{\mathbf{p}_1, \mathbf{p}_2, \dots, \mathbf{p}_{N_p}\}$, where $\mathbf{p}_i \in \mathbb{R}^2$.

4.3 Speed Planner

To efficiently navigate a planned path, the speed planner generates a speed profile for each checkpoint. This process is formulated as a constrained optimization problem,

aiming to minimize the total travel time. The variables in this optimization problem are the speed profiles for each checkpoint, denoted as $\{v_1, v_2, \dots, v_{N_p}\}$. The objective function is given by the equation,

$$\text{Time} = \sum_{i=1}^{N_p-1} \frac{2\|\mathbf{p}_{i+1} - \mathbf{p}_i\|}{v_{i+1} + v_i}. \quad (43)$$

Several constraints are imposed on the speed profile to ensure safe and feasible navigation. They are derived from the terrain properties, vehicle capabilities, and trajectory shape. Specifically, four types of constraints are considered.

Force Constraint ensures the force required to accelerate, climb, and steer does not exceed the maximum friction the terrain can provide. Consider the checkpoint \mathbf{p}_i , denote the nearby friction coefficient as μ_i , the angle of slope as θ_i , the radius of curvature as r_i , and the terrain roughness as σ_i . Therefore, the maximum friction available is

$$F_f^i = \mu_i M g \cos \theta_i. \quad (44)$$

The centripetal force required for steering is

$$F_c^i = M \cdot \frac{v_i^2}{r_i}. \quad (45)$$

The force counteracting the gravity along the slope is

$$F_s^i = -M g \sin \theta. \quad (46)$$

The force used to accelerate is

$$F_a^i = -M \cdot \frac{(v_{i+1} - v_i)(v_{i+1} + v_i)}{2\|\mathbf{p}_{i+1} - \mathbf{p}_i\|}. \quad (47)$$

To maintain control, the maximum available friction must be at least equal to the total forces required, therefore

$$\forall i, F_f^i \geq \sqrt{(F_c^i)^2 + (F_s^i + F_a^i)^2}. \quad (48)$$

Traction Constraint sets a threshold on maximum traction force F_{th} based on the vehicle engine's capability,

$$\forall i, F_s^i + F_a^i \leq F_{th}. \quad (49)$$

Roughness Constraint sets a velocity threshold based on the terrain roughness,

$$\forall i, v_i \leq \phi(\sigma_i), \quad (50)$$

where $\phi(\cdot)$ is an empirical function mapping roughness to the maximum allowed speed, based on vehicles' passability.

Velocity Constraint ensures the start and end velocities are zero, and all other velocities are positive.

$$\begin{aligned} v_1 = v_{N_p} &= 0, \\ v_i &> 0, \quad \forall 1 < i < N_p. \end{aligned} \quad (51)$$

To solve this constrained optimization problem, we employ the Sequential Least Squares Programming (SLSQP) algorithm (Kraft 1988), resulting in an optimal speed profile for each checkpoint along the path.

5 Experiments

We next evaluate the effectiveness of the proposed neuro-symbolic friction learning framework in Section 5.2, physics-infused path planning in Section 5.3, and validate their real-world performance in Section 5.4.

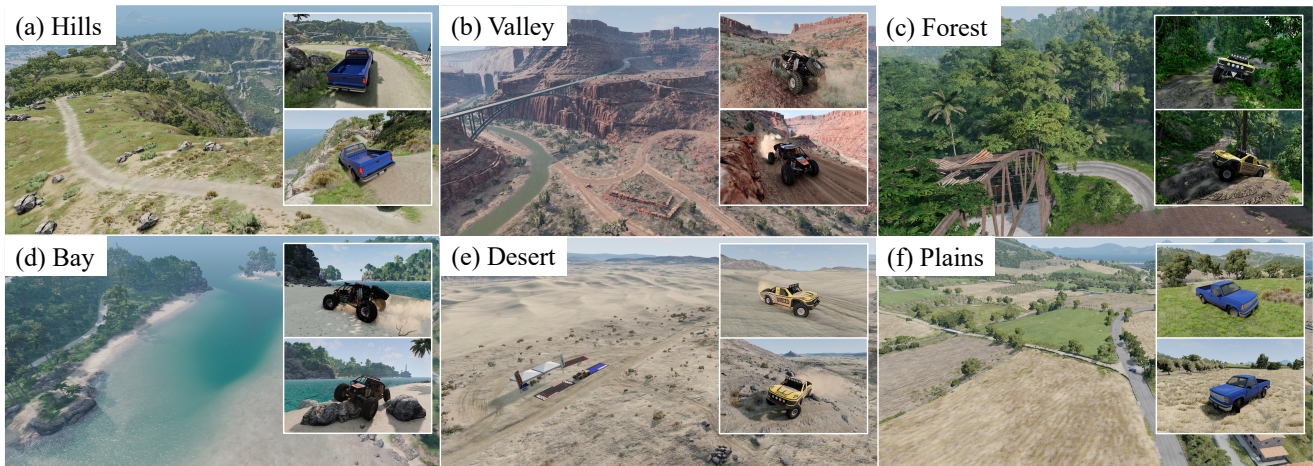


Figure 8. Driving data collection in six simulated environments, each features diverse terrain types and unique friction properties.



Figure 9. Real-world data collection conducted across various terrains, including grass, gravel, cement, and mud.

5.1 Experimental Setup

5.1.1 Simulated Environments We utilize BeamNG.tech (BeamNG GmbH 2022) as our driving simulator due to its high-fidelity modeling of vehicle-terrain interactions and realistic visual rendering, which helps reduce the sim-to-real gap. Besides, the simulator also provides a diverse array of environments and a broad selection of vehicles, which is important to test the system’s generalizability. As illustrated in Figure 8, we use six virtual environments, *plains, desert, bay, hills, forest, and valley*. Each terrain type features unique friction properties that influence the vehicle’s dynamics during driving. Three vehicles, *pickup, race truck, and rock climber* are driven in both *autopilot mode* and *manual mode*. In the *autopilot mode*, the vehicles are driven by BeamNG’s built-in AI driver, following predefined paths. It features professional-level smooth accelerating, braking, and steering. In *manual mode*, the vehicles are driven by a human player. It features more aggressive driving such as full throttle acceleration and long drifting.

5.1.2 Real-World Environments We leverage the open-source TartanDrive dataset (Triest et al. 2022) along with our own dataset collected using a rover robot to conduct real-world experiments. TartanDrive provides high-quality off-road driving data collected using a Yamaha ATV. It includes a comprehensive sensor suite providing various sensor modalities. Our rover dataset is collected on the

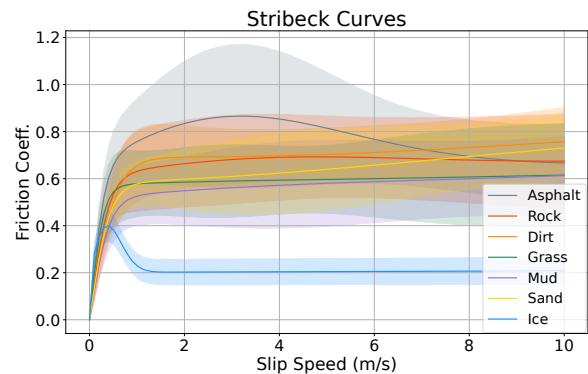


Figure 10. Predicted Stribeck curves for each terrain type, with mean values plotted as solid lines and standard deviations shaded as transparent regions.

North Campus of the University at Buffalo, featuring diverse terrains and significant slopes, as illustrated in Figure 9. The rover is customized from the Aion R1 model. While the simulated vehicles and TartanDrive’s ATV utilize Ackermann steering, which steers by rotating the two front wheels, our rover employs differential steering, turning via the speed difference between its left and right wheels. Notably, our model can be seamlessly deployed on the rover, as the predicted physical parameters are adaptable to any vehicle configuration, verifying our system’s generalizability.

5.1.3 Data Preprocessing Both the simulated and real-world datasets include synchronized front camera images, LiDAR scans, IMU measurements, and wheel RPM data. The simulated dataset additionally provides ground truth poses, velocities, and terrain-type segmentation. For the real-world data, we apply a LiDAR-inertial SLAM algorithm, SuperOdometry (Zhao et al. 2021) to estimate the vehicle’s trajectory. The LiDAR point clouds are colorized, aggregated, and down-sampled to create a point-cloud map, from which bird’s-eye-view patches are cropped. We randomly split both the simulated dataset and the rover dataset into 80% for training, 10% for validation, and 10% for testing, while adhering to the same data split for TartanDrive (Triest et al. 2022) as suggested in the paper.

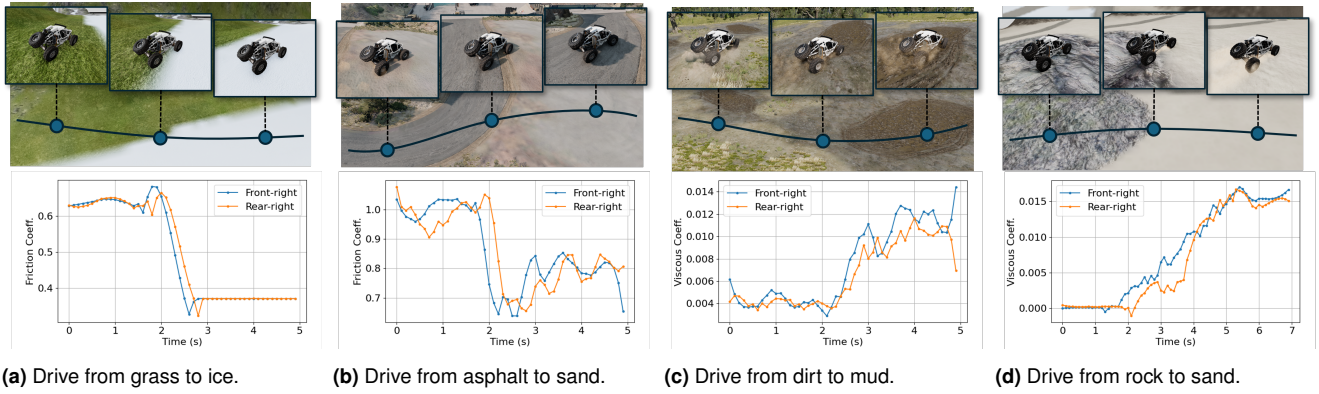


Figure 11. Variation of friction coefficients (a, b) and viscous coefficients (c, d) when driving from one terrain type to another.

Table 1. Comparison of ATE, RRE, and RTE on the simulated dataset. Trajectories are categorized by their traversed terrain types.

	TartanDrive			PhysORD			UKF (Vosahlik et al. 2021)			PF (Vosahlik et al. 2021)			AnyNav (Ours)		
	ATE	RRE	RTE	ATE	RRE	RTE	ATE	RRE	RTE	ATE	RRE	RTE	ATE	RRE	RTE
Asphalt	2.230	27.405	4.479	1.318	28.334	2.594	2.230	27.405	4.479	2.198	17.191	4.483	0.725	9.700	1.523
Rock	2.108	42.280	4.340	1.444	32.495	3.026	2.108	42.280	4.340	1.939	24.183	3.875	0.453	11.310	0.943
Dirt	1.992	28.958	4.193	1.037	34.120	2.215	1.992	28.958	4.193	1.712	29.041	3.611	0.685	8.116	1.392
Grass	2.387	33.816	4.825	0.890	39.178	1.945	2.387	33.816	4.825	2.162	26.090	4.333	0.523	9.153	1.062
Mud	1.631	34.449	3.467	1.290	35.444	2.709	1.631	34.449	3.467	1.387	21.405	2.885	0.664	19.480	1.461
Sand	1.728	18.600	3.484	1.161	25.111	2.339	1.728	18.600	3.484	1.554	20.735	3.095	0.630	11.032	1.283
Ice	1.028	12.497	2.060	1.068	24.882	2.213	1.028	12.497	2.060	0.679	15.841	1.269	0.322	7.567	0.635
Overall	1.833	27.490	3.752	1.195	30.724	2.465	1.833	27.490	3.752	1.633	21.064	3.306	0.583	11.420	1.216

5.2 Friction Learning Evaluation

In this section, we present the evaluation of the proposed neuro-symbolic friction learning module. We begin with a qualitative analysis of the learned Stribeck coefficients across terrain types in Section 5.2.1. As the ground truth friction is not directly measurable, we instead perform evaluations on trajectory estimation in Section 5.2.2 and kinematic prediction in Section 5.2.3, using the precision of these tasks as an indirect measure of the accuracy of friction predictions. The ablation study on the effectiveness of our dual-loss and bilevel optimization is presented in Section 5.2.4

5.2.1 Qualitative Analysis The learned Stribeck curves in simulated environments are displayed in Figure 10. Using the provided semantic labels, we aggregate the results into seven categories and plot the mean and variance of the friction coefficient as a function of slip speed. Note that these categories are only used for visualization, not in training. The *asphalt* category exhibits the highest overall friction, while *ice* has the lowest, which is consistent with common sense.

We next show the change of predicted friction coefficient and the viscous coefficient on individual wheels between their transition across terrain types in Figure 11. As observed, the friction coefficient drops significantly when transitioning from *grass* to *ice* and from *asphalt* to *sand*, while the viscous coefficient increases when transitioning from *dirt* to *mud* and from *rock* to *sand*, verifying the effectiveness of our method.

5.2.2 Trajectory Estimation We next evaluate the accuracy of the estimated trajectory $\{\xi_i^{est}\}_{i=1}^N$ from the symbolic reasoning engine. Following Zhao et al. (2024)’s work, we set steps $N = 20$ and use Absolute Trajectory Error (ATE), Relative Rotation Error (RRE), and Relative Translation Error (RTE) as metrics. The RRE and RTE are evaluated at

Table 2. Errors of trajectory estimation on real-world data.

	TartanDrive			Rover		
	ATE	RRE	RTE	ATE	RRE	RTE
TartanDrive	0.754	5.234	0.771	0.187	38.72	0.368
PhysORD	0.674	5.119	0.586	0.179	19.71	0.354
UKF	0.877	4.986	1.800	0.227	29.74	0.458
PF	0.649	7.320	1.232	0.167	26.01	0.332
AnyNav (Ours)	0.310	2.349	0.543	0.084	4.837	0.143

the last time step. The results are compared against state-of-the-art learning-based methods, TartanDrive (Triest et al. 2022) and PhysORD (Zhao et al. 2024), as well as Vosahlik et al. (2021)’s Unscented Kalman Filter (UKF)-based method and its Particle Filter (PF) variant. Table 1 presents the results on our simulated dataset, where trajectories are categorized by their predominant terrain types. It is observed that our method outperforms all competitors across all terrain types. Table 2 summarizes the results on two real-world datasets, showing that our approach consistently outperforms all competitors in real-world scenarios. Since our trajectories are physically computed based on the estimated friction coefficients, the high accuracy in trajectory estimation reflects the precision of our friction prediction.

5.2.3 Kinematic Prediction Another way to validate the accuracy of the estimated friction coefficient is to use these estimations to predict the future kinematics of the vehicle under specific conditions and compare the predictions with the actual outcomes observed in the simulator or real-world experiments. Following this principle, we designed a steering test and a slope climbing test.

Steering Test in Simulator In this experiment, we use the trained neural network to predict Stribeck coefficients S_{pred}^u for different terrain types u , and use these predictions

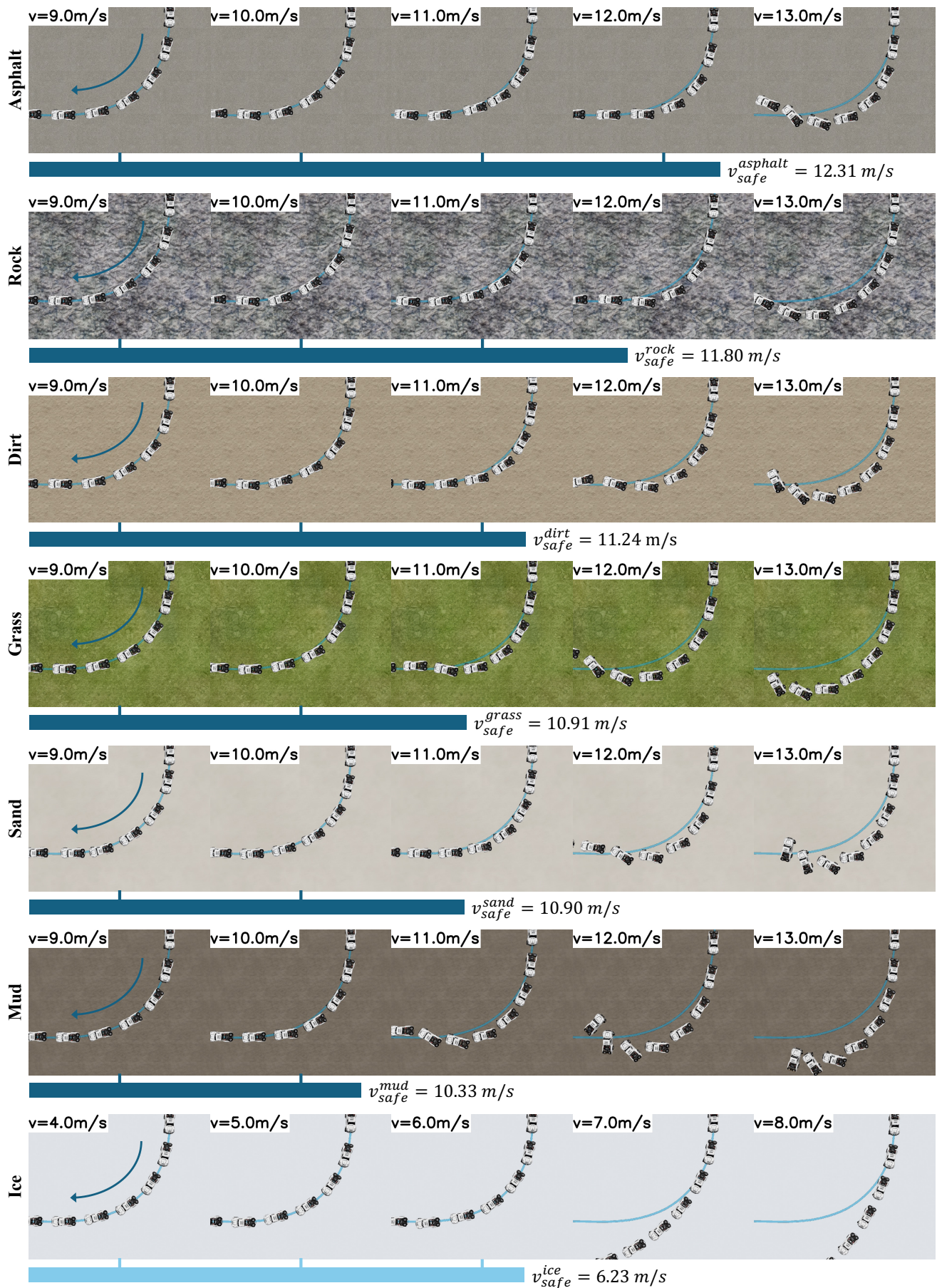


Figure 12. Top-down views of steering experiments conducted at varying speeds across different terrains. The results show that the predicted maximum safe speed v_{safe} accurately distinguishes between driftless steering and drifting scenarios.

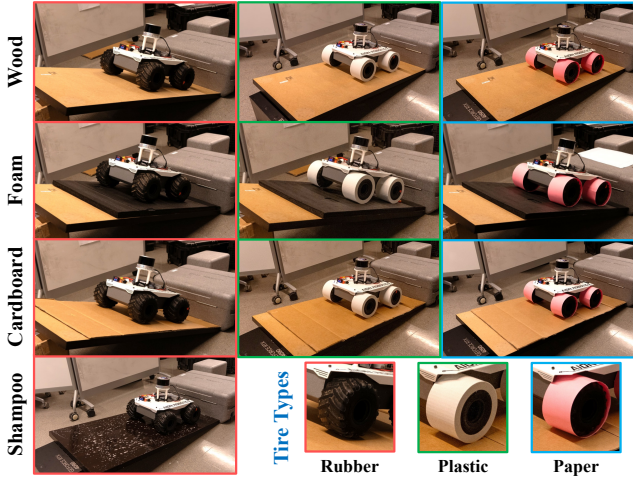


Figure 13. Experimental setup for the slope-climbing test: conducted on four different surface materials using three types of tires, creating a large range of friction conditions.

Table 3. The predicted and measured maximum climb angles (in degrees) across various ground and wheel materials.

	Rubber		Plastic		Paper	
	Pred.	Meas.	Pred.	Meas.	Pred.	Meas.
Wood	39.2	43	15.8	16	13.4	14
Foam	41.2	46	23.9	23	27.9	25
Cardboard	39.7	44	11.1	10	11.0	12
Shampoo	16.4	15	-	-	-	-

to calculate the maximum safe speed v_{safe}^u , at which a vehicle can complete a turn with a specified radius of curvature r without experiencing significant drift. According to kinematic principles, the centripetal force during steering is provided by friction force,

$$M \frac{(v_{safe}^u)^2}{r} = \mu_{pred}^u \cdot Mg \Rightarrow v_{safe}^u = \sqrt{rg\mu_{pred}^u}, \quad (52)$$

where $\mu_{pred}^u = \text{Stribeck}(v_{rel}; S_{pred}^u)$. To validate these predictions, we conduct steering tests at various speeds in the simulator. We pick a typical slip speed of $v_{rel} = 1m/s$ and set the turning radius to $r = 20m$ for all tests. The simulation results, along with the predicted safe speeds, are visualized in Figure 12. It is observed that trial speeds exceeding v_{safe}^u result in significant drift or even failure to complete the turn, whereas trial speeds below v_{safe}^u allow the turn to be successfully completed. This outcome highlights both the accuracy of the predicted friction coefficients and their clear physical relevance in modeling terrain-specific dynamics.

Slope Climbing Test in the Real World The objective of this experiment is to predict whether a vehicle can climb a certain slope based on estimated friction coefficients. Specifically, we calculate the maximum slope angle θ_{max}^u that a vehicle can ascend on certain ground type u ,

$$\mu_{pred}^u \cdot Mg \cos \theta_{max}^u = Mg \sin \theta_{max}^u \Rightarrow \theta_{max}^u = \arctan(\mu_{pred}^u), \quad (53)$$

where μ_{pred}^u is estimated friction coefficient via the lower-level optimization introduced in Section 3.3.2. The optimization is performed on a sequence of 3-5 minutes driving data on ground type u . We conducted real-world tests on slopes with different surface materials, including

wood, foam, cardboard, and a shampoo-covered board. To further assess generalizability, we replaced the standard rubber tire surface with alternative materials such as plastic (3D printed) and paper. The experimental setups are shown in Figure 13. The results, summarized in Table 3, indicate that the predicted angles align well with the observed outcomes. Notably, the predictions are more accurate for low-friction surfaces. This is because the vehicle exhibits more pronounced slipping when friction is low, providing a greater number of valid data points for learning the Stribeck curve. This experiment validated that the lower-level optimization can accurately estimate friction coefficients from driving data, providing high-quality pseudo-labels for the neural module to learn from real-world environments.

5.2.4 Ablation Studies We conducted an ablation study on the training losses by comparing the ATE, RRE, and RTE when using only the dynamics loss, only the prior knowledge loss, and both losses together. The results, presented in Table 4, show that using both losses yields better performance compared to using either loss individually. This highlights the complementary nature of the two loss components in improving overall model accuracy.

Table 4. Ablation study of dynamics loss L_d and prior knowledge loss L_p for training in the simulator.

	ATE	RRE	RTE
L_d Only	0.685	15.558	1.394
L_p Only	0.658	14.839	1.405
AnyNav (Ours)	0.583	11.420	1.216

We also conducted an ablation study on the fine-tuning process designed to adapt to real-world scenarios. During lower-level optimization, we separately fixed the wheel speed to its noisy raw measurements and the vehicle’s inertia matrix to its initial guess, instead of optimizing them together. Additionally, we evaluated the performance of the model trained in simulation without any fine-tuning. The results, summarized in Table 5, show that our method outperforms all these variations, highlighting the effectiveness of jointly optimizing all factors.

Table 5. Ablation study comparing no fine-tuning, fixed wheel speed measurements during fine-tuning, and fixed vehicle’s rotational inertia matrix during fine-tuning.

	TartanDrive Dataset			Rover Datasets		
	ATE	RRE	RTE	ATE	RRE	RTE
Without fine-tuning	0.68	4.45	1.21	0.10	10.8	0.17
Fix wheel speed	0.66	3.99	1.18	0.10	7.10	0.18
Fix inertia matrix	0.37	3.48	0.64	0.09	8.93	0.16
AnyNav (Ours)	0.31	2.35	0.54	0.08	4.84	0.14

5.3 Path Planning Assessment

In this section, we evaluate our planning system in terms of the feasibility of planned paths, the efficiency of speed profiles, and its robustness under complex environments.

5.3.1 Navigation Environments and Vehicle Controller We utilize two environments in BeamNG for planning assessments, namely *Garden* and *Island* in Figure 14. It is

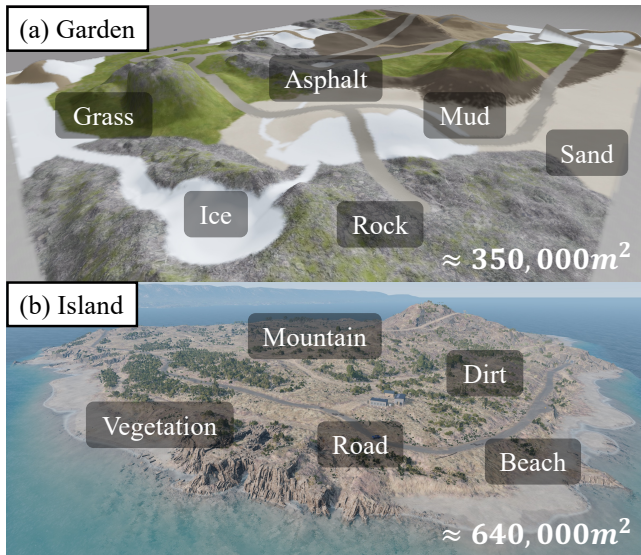


Figure 14. The two environments for planning assessment.

worth noting that the two environments are not seen during training in order to test the generalizability. The *Garden*, designed specifically for this study by ourselves, features diverse terrain types and a variety of slopes. It includes challenging regions such as ice-covered mountains and muddy basins to test the planner’s robustness. The *Island* is a built-in map in BeamNG that features high mountains, rocky cliffs, and uneven dirt grounds with bushes and trees. The sparse roads in this map present the planner with strategic choices, such as taking a flatter but longer road or opting for a shorter but more difficult off-road trail. Its realistic terrain closely mimics real-world conditions, providing a valuable benchmark for evaluating the planner. Additionally, we employ a simple PD controller to control the vehicle’s throttle, brake, and steering in real-time, ensuring accurate execution of the planned trajectory and speed.

5.3.2 Demonstrations For comparison, we include trajectories planned without friction predictions to validate the effectiveness of incorporating physics-based information into our planner. For better visualization, we present two exemplary planning results for each environment.

Figure 15 illustrates a navigation task in the *Garden*, where the target point is located atop an icy crater. Without considering the terrain-specific friction properties, the planner selects a shorter route through the icy valley (red line). This choice results in navigation failure, as the icy region is too slippery for the vehicle to ascend (green arrows). In contrast, our physics-infused planner, which reasons about both friction levels and slope angles, selects a detour that avoids most of the icy regions and utilizes high-friction rocky areas to ascend (blue line). This physically feasible route allows the vehicle to successfully reach the target. This example highlights the robustness and reliability of our physics-infused planner under challenging conditions.

Figure 16 illustrates another navigation task in the *Garden*. The planner without friction knowledge selects a shorter route across the sand (red line), while our physics-infused planner generates a longer path on an asphalt road (blue line). This decision is based on the planner’s

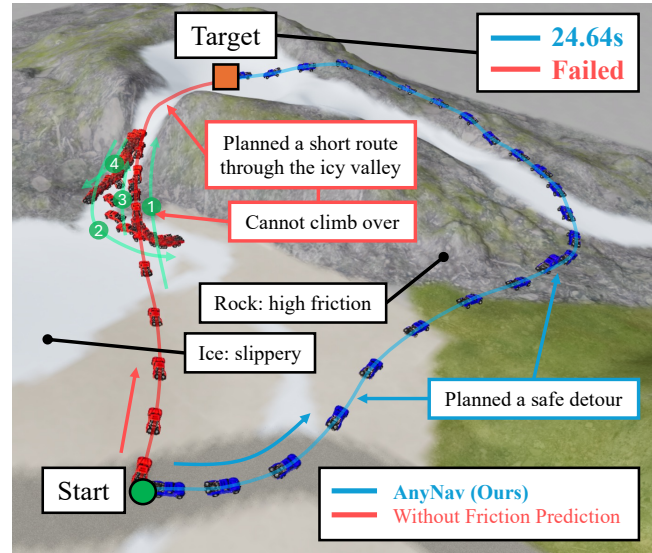


Figure 15. A navigation task where the target is atop an icy crater. The planner without friction prediction (red) attempted to plan a shorter path but failed due to the low friction in the icy valley. In contrast, our planner (blue) suggests a safe detour with enough friction, successfully completing the task.

understanding that sand is more slippery and has higher resistance, while asphalt road allows for higher average speed. As a result, our planned route achieves 11.1% faster by considering physical knowledge. This example highlights the advantage of incorporating physics-based friction predictions for optimizing travel time.

Figure 17 showcases two tasks performed in the *Island*. Task 1, similar to the previous example in *Garden*, demonstrates that our planner consistently identifies the efficient route in terms of travel time using a physics-based approach. Task 2 highlights the effectiveness of our steering-minimization design. Without the steering cost, the planned path is more winding (yellow line), which reduces the vehicle’s average speed. In contrast, our steering-minimized planner results in a smoother path with more straight segments which is 14.7% faster. This highlights the effectiveness of our approach in accounting for steering by significantly enhancing overall travel efficiency.

5.3.3 Quantitative Evaluation We next present a quantitative evaluation to further validate the high performance of our physics-infused planner. We randomly generated 100 navigation tasks, with 50 tasks on each map. Several examples of the planned paths are shown in Figure 18.

Metrics Three metrics, i.e., success rate, average time, and time ratio are used to evaluate our system. Specifically, the success rate represents the percentage of completed tasks out of the total; average time refers to the mean travel time for completed tasks; and time ratio is defined as the ratio of actual travel time to predicted travel time. Intuitively, a time ratio significantly greater than 1 indicates that the planned speed is too high for the vehicle to achieve.

Baselines We evaluated our method against four groups of baselines to provide a comprehensive analysis of its advantages in various aspects. The first group of baselines involves planning methods based on traversability maps.

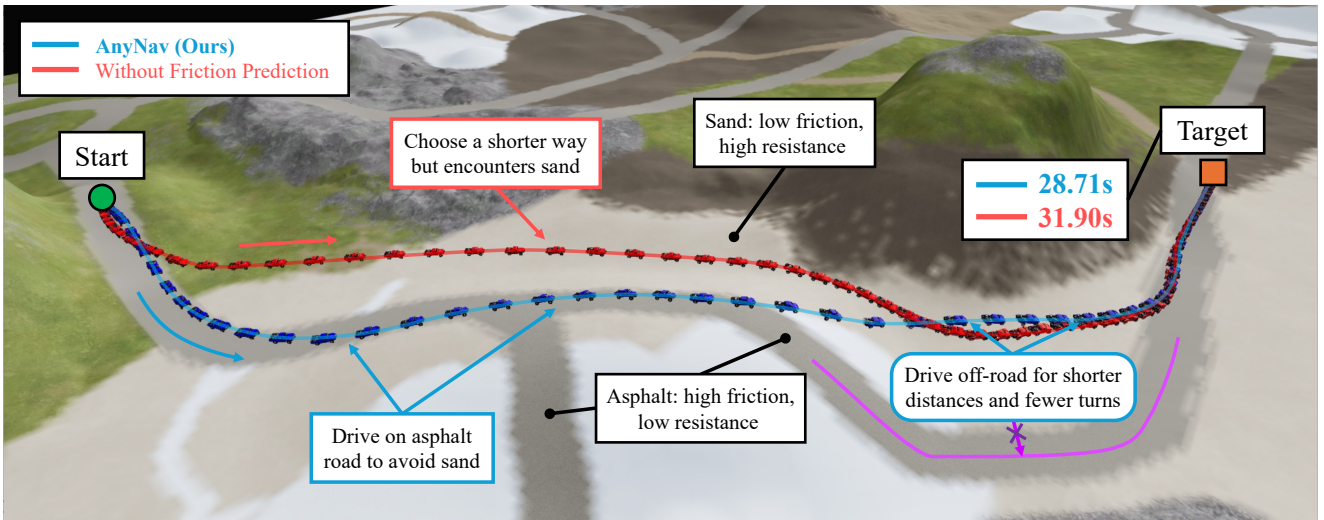


Figure 16. An example highlights the advantage of our planner, which optimizes travel time by selecting a low-resistance route.

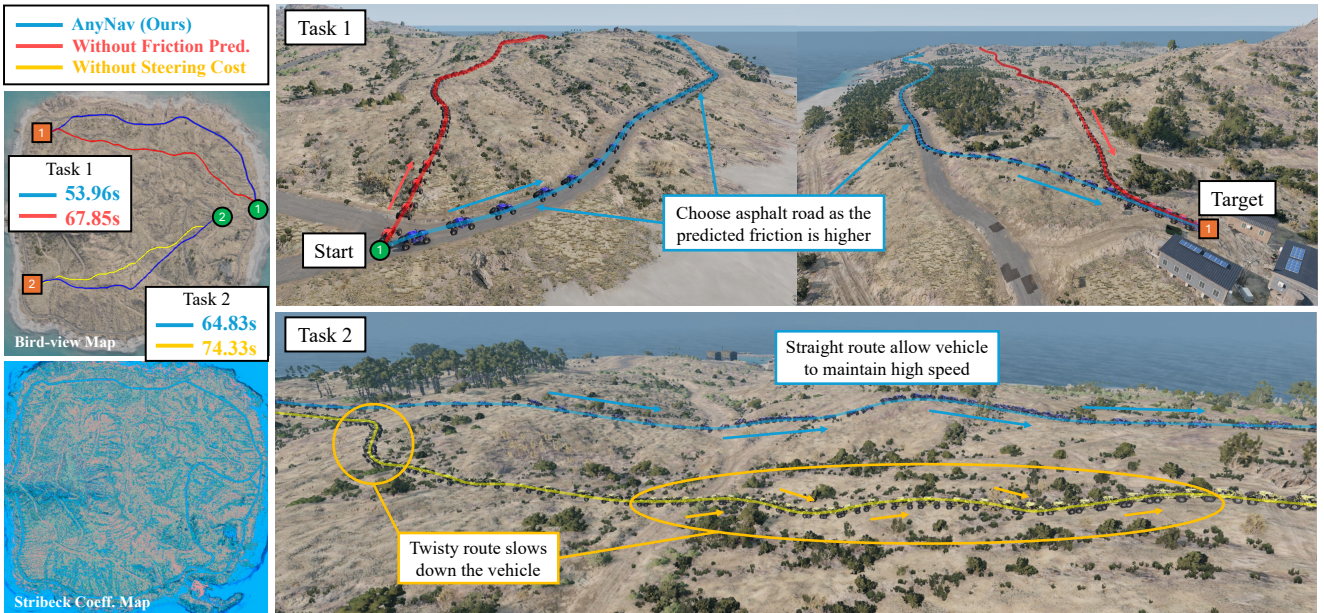


Figure 17. Two navigation examples on the *Island* map. Task 1 highlights how incorporating friction knowledge into planning reduces travel time. Task 2 showcases the efficiency of our steering-minimized strategy in improving average speed.

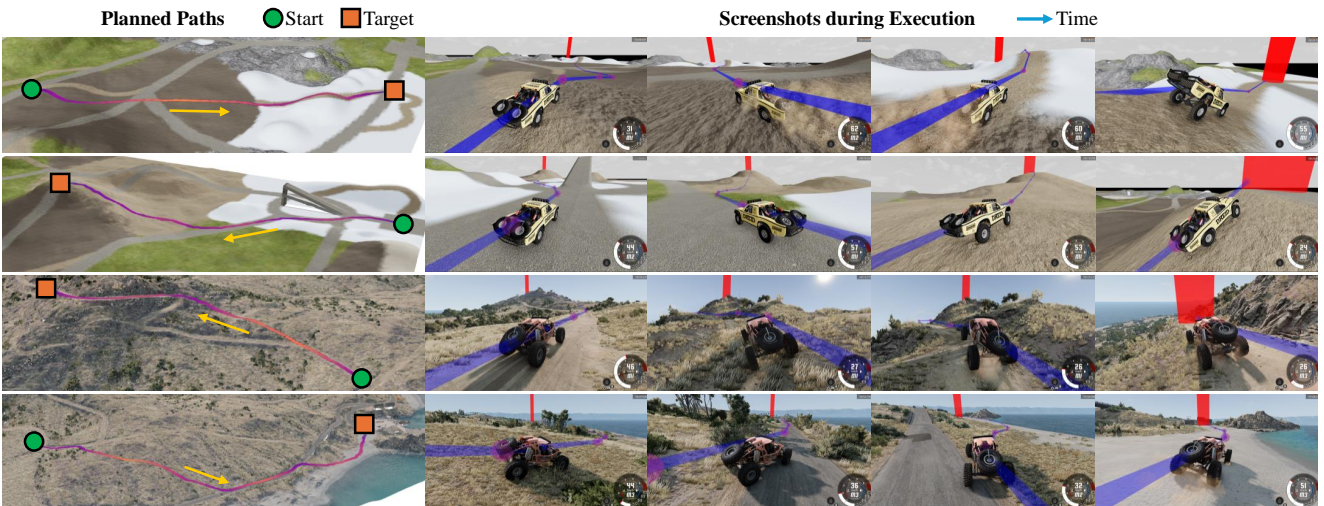


Figure 18. Examples of planned paths in two environments, along with screenshots captured during execution in the simulator.

Table 6. Comparison of Success Rate, Average Time, and Time Ratio across two Maps. Note that the Average Time and Time Ratio is computed only on successful tasks. The best Success Rates are marked in bold.

		Garden			Island		
		Succ. Rate	Avg. Time	Time Ratio	Succ. Rate	Avg Time	Time Ratio
Traversability -based	binary	72%	31.661	1.116	60%	46.544	1.208
	URA*	26%	53.774	-	8%	62.605	-
Modify friction	$\mu = 0.2$	90%	42.820	0.969	92%	73.678	0.962
	$\mu = 0.5$	82%	29.765	1.078	92%	46.183	1.063
	$\mu = 0.8$	82%	28.197	1.127	82%	42.408	1.208
	$0.5\mu_{pred}$	100%	39.260	0.997	92%	55.217	1.004
	$1.5\mu_{pred}$	86%	29.620	1.158	74%	38.569	1.181
Scale velocity	$0.75v$	100%	35.830	0.942	94%	49.620	0.986
	$1.25v$	82%	27.638	1.230	80%	38.032	1.286
Without steering cost		96%	32.304	1.064	88%	44.405	1.083
AngNav (Ours)		100%	29.648	1.037	94%	41.942	1.099

We first implement an approach similar to Ramirez-Robles et al. (2024), generating a binary traversability map in which obstacles and icy ground are marked as non-traversable. Paths are then planned using the standard A* algorithm to avoid these areas. This baseline is referred to as “binary”. Additionally, we implemented URA* (Moore et al. 2023), which uses a learning-based method to identify traversable and non-traversable regions from BEV images, followed by an A*-like algorithm for route planning. The second group of baselines examines the impact of modifying the friction information provided to the planner. In the first three baselines, the friction coefficient is set to constant values of 0.2, 0.5, and 0.8 across the entire map, eliminating any terrain-specific information. In the latter two baselines, our predicted friction coefficients are scaled by factors of 0.5 and 1.5, respectively, verifying the effects of inaccurate friction predictions for the planner. The third group of baselines adjusts our planned speed by directly scaling it by factors of 0.75 and 1.25, respectively. The fourth baseline excludes the steering cost from the planning process.

Results The experimental results are presented in Table 6. Compared to the traversability-based baselines, our planner achieves higher success rates and lower average travel times. This demonstrates its state-of-the-art performance, achieved by leveraging continuous values to represent physics-infused traversability, rather than relying on binary obstacle maps.

Compared to baselines with modified friction information, it is observed that all such modifications result in decreases in success rates and increases in average travel times. Specifically, when the friction coefficient is set to a low value (e.g. $\mu = 0.2$ or $0.5\mu_{pred}$), the planner becomes overly cautious, resulting in significantly reduced planned speeds and therefore increased average travel times. Conversely, when the friction coefficient is set to a high value (e.g. $\mu = 0.8$ or $1.5\mu_{pred}$), the planner becomes overly confident, leading to aggressive plans that cause a significant drop in success rate. These outcomes demonstrate both the accuracy of our friction predictions and the planner’s ability to utilize these predictions to generate safe and efficient paths.

Compared to baselines with scaled speed profiles, using our planned speed achieves a higher success rate and shorter average time overall. Note that average

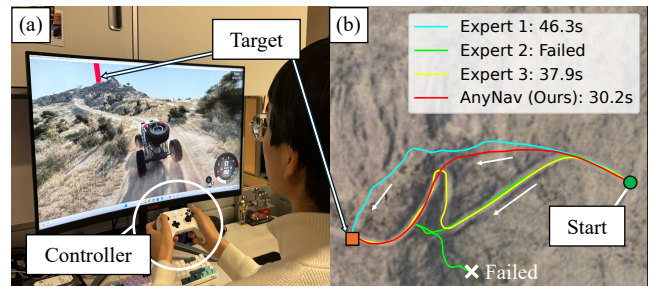


Figure 19. Compete with Human Experts. (a) The human driver uses an Xbox controller to operate the vehicle toward the target, which is marked by a tall red cylinder on the screen. (b) In one example task, Expert 2 failed while attempting to climb a steep slope and fell off; Experts 1 and 3 successfully reached the target but took longer than our planner.

time is calculated only for successful plans, making it a meaningful comparison only when success rates are similar. These results demonstrate that our planned speed is nearly optimal: deviating from it leads to a drop in performance. Additionally, the time ratio for the $1.25v$ baseline is significantly greater than 1, while that for ours is approximately 1. This indicates that our planned speed effectively leverages the terrain’s friction while remaining within the vehicle’s operational limits.

Compared to the baseline that excludes the steering cost, our method also achieved a shorter average travel time. This highlights the effectiveness of our steering-minimization strategy in enhancing overall navigation efficiency.

5.3.4 Compete with Human Experts To further evaluate the reliability and efficiency of our physics-infused planner,

Table 7. Comparison of AnyNav with Human Experts.

	Garden		Island	
	Succ. Rate	Avg. Time	Succ. Rate	Avg. Time
Expert 1	90%	30.864	60%	47.150
Expert 2	100%	31.524	70%	43.785
Expert 3	100%	29.429	90%	45.154
AnyNav (Ours)	100%	27.995	100%	40.402



Figure 20. Real-world deployment of our AnyNav system. (a) The environment map is collaboratively reconstructed by a rover and a drone. (b) The Stribeck coefficient is estimated using the neuro-symbolic module. (c-e) Multiple navigation tasks are executed using the AnyNav planner. The red points are selected target locations and the blue lines are planned trajectories.

we conducted an experiment to compare its performance against human experts in navigating challenging terrains. Human experts were tasked with manually controlling the vehicle using an Xbox controller to complete the same set of navigation tasks. A total of 20 tasks were randomly selected, with 10 tasks on each map. Before starting, the human experts were given 1 minute to examine a 3D mesh of the terrain to familiarize themselves with the environment. During each test, the vehicle was spawned at the starting point, and the target location was marked with a tall red cylinder, visible from anywhere on the map. The sample setup is shown in Figure 19(a). The drivers were instructed to drive the vehicle to the target as quickly as possible. A task was deemed a failure if the vehicle tipped over or remained stuck for more than 5 seconds. An example task is shown in Figure 19(b), where human experts either failed or took longer to reach the target compared to our planner. The full results are summarized in Table 7, showing that our planner achieves a higher success rate and shorter average time compared to all human experts on both maps.

5.4 Real-World Deployment

We deployed AnyNav in a real-world application, as illustrated in Figure 20, where environmental observations were collaboratively collected by a rover and a drone. The rover was equipped with a LiDAR-inertial SLAM system, SuperOdometry (Zhao et al. 2021), for localization and mapping. These point clouds were colorized using RGB images captured by the rover’s front camera. We implemented a real-time mapping system utilizing the quadtree data structure for flexible multi-robot collaborative reconstruction. It supports dynamic update and expansion as new observations are made, while also automatically offloading inactive regions to disk to save memory. The data from both sources were integrated into this mapping system, producing the final reconstruction shown in Figure 20(a). The Stribeck coefficients were estimated using our neuro-symbolic module, shown in Figure 20(b), with input data obtained from the mapping system. The elevation and roughness map layers were computed as in Section 4.1.

During operation, users selected several points of interest on the BEV map. The point coordinates were then

transmitted to the rover, where our physics-infused planner generated trajectories for traversing sequentially. The rover is then controlled by a PD controller to follow the planned path at the desired velocity, as shown in Figure 20(c-e). Our system efficiently guides the vehicle to its targets by avoiding obstacles and selecting routes with gentler slopes. This experiment demonstrates the system’s adaptability and effectiveness in real-world scenarios.

6 Limitation & Conclusion

In this paper, we present AnyNav, a physics-grounded framework for off-road navigation. It combines a neuro-symbolic approach for learning terrain friction coefficients with a physics-infused planner that leverages friction knowledge for path and speed planning. Experiments conducted in both simulation and real-world settings demonstrate the accuracy of our friction prediction model and the robustness of our planning system. These results highlight progress toward creating neuro-symbolic spatial intelligence that can effectively interpret complex, unstructured environments and enable reliable autonomous navigation in challenging off-road scenarios. While this paper primarily focuses on incorporating friction coefficients into the planner, other terrain properties, such as stiffness, elasticity, and plasticity, are worth further research.

Acknowledgements

This work was, in part, funded by DARPA grant DARPA-PS-23-13 and ONR award N00014-24-1-2003. The views and conclusions contained in this document are those of the authors and should not be interpreted as representing the official policies, either expressed or implied, of DARPA or ONR. The authors also thank Bowen Li (Carnegie Mellon University) for the insightful discussions.

References

- Agishev R, Zimmermann K, Pecka M and Svoboda T (2023) Monoforce: Self-supervised learning of physics-aware grey-box model for predicting the robot-terrain interaction. [arXiv preprint arXiv:2309.09007](https://arxiv.org/abs/2309.09007).
- Ailon A, Berman N and Arogeti S (2005) On controllability and trajectory tracking of a kinematic vehicle model. *Automatica* 41(5): 889–896.

- Armstrong B and de Wit C (1995) Canudas, "friction modeling and compensation", the control handbook.
- BeamNG GmbH (2022) BeamNG.tech. URL <https://www.beamng.tech/>.
- Brandao M, Shiguematsu YM, Hashimoto K and Takanishi A (2016) Material recognition cnns and hierarchical planning for biped robot locomotion on slippery terrain. In: 2016 IEEE-RAS 16th International Conference on Humanoid Robots (Humanoids). IEEE, pp. 81–88.
- Cai X, Queeney J, Xu T, Datar A, Pan C, Miller M, Flather A, Osteen PR, Roy N, Xiao X and How JP (2024) Pietra: Physics-informed evidential learning for traversing out-of-distribution terrain. arXiv preprint arXiv:2409.03005 .
- Castro MG, Triest S, Wang W, Gregory JM, Sanchez F, Rogers JG and Scherer S (2023) How does it feel? self-supervised costmap learning for off-road vehicle traversability. In: 2023 IEEE International Conference on Robotics and Automation (ICRA). IEEE, pp. 931–938.
- Chen J, Frey J, Zhou R, Miki T, Martius G and Hutter M (2024) Identifying terrain physical parameters from vision-towards physical-parameter-aware locomotion and navigation. IEEE Robotics and Automation Letters .
- Chen RT, Rubanova Y, Bettencourt J and Duvenaud DK (2018) Neural ordinary differential equations. Advances in neural information processing systems 31.
- Di X and Shi R (2021) A survey on autonomous vehicle control in the era of mixed-autonomy: From physics-based to ai-guided driving policy learning. Transportation research part C: emerging technologies 125: 103008.
- Duruissieux V, Duong TP, Leok M and Atanasov N (2023) Lie group forced variational integrator networks for learning and control of robot systems. In: Learning for Dynamics and Control Conference. PMLR, pp. 731–744.
- Ewen P, Chen H, Chen Y, Li A, Bagali A, Gunjal G and Vasudevan R (2024) You've got to feel it to believe it: Multi-modal bayesian inference for semantic and property prediction. arXiv preprint arXiv:2402.05872 .
- Ewen P, Li A, Chen Y, Hong S and Vasudevan R (2022) These maps are made for walking: Real-time terrain property estimation for mobile robots. IEEE Robotics and Automation Letters 7(3): 7083–7090.
- Frey J, Khattak S, Patel M, Atha D, Nubert J, Padgett C, Hutter M and Spieler P (2024) Roadrunner-learning traversability estimation for autonomous off-road driving. arXiv preprint arXiv:2402.19341 .
- Greydanus S, Dzamba M and Yosinski J (2019) Hamiltonian neural networks. Advances in neural information processing systems 32.
- Hart PE, Nilsson NJ and Raphael B (1968) A formal basis for the heuristic determination of minimum cost paths. IEEE transactions on Systems Science and Cybernetics 4(2): 100–107.
- Havens A and Chowdhary G (2021) Forced variational integrator networks for prediction and control of mechanical systems. In: Learning for Dynamics and Control. PMLR, pp. 1142–1153.
- Huber PJ (1992) Robust estimation of a location parameter. In: Breakthroughs in statistics: Methodology and distribution. Springer, pp. 492–518.
- Islam F, Nabi M and Ball JE (2022) Off-road detection analysis for autonomous ground vehicles: A review. Sensors 22(21): 8463.
- Kraft D (1988) A software package for sequential quadratic programming. Forschungsbericht- Deutsche Forschungs- und Versuchsanstalt für Luft- und Raumfahrt .
- Liu M, Cao W and Fan Z (2004) Convergence and stability of the semi-implicit euler method for a linear stochastic differential delay equation. Journal of Computational and Applied Mathematics 170(2): 255–268.
- Madsen J, Negrut D, Reid A, Seidl A, Ayers P, Bozdech G, Freeman J and O'Kins J (2012) A physics-based vehicle/terrain interaction model for soft soil off-road vehicle simulations. SAE International Journal of Commercial Vehicles 5(2012-01-0767): 280–290.
- Moore C, Mitra S, Pillai N, Moore M, Mittal S, Bethel C and Chen J (2023) Ura*: Uncertainty-aware path planning using image-based aerial-to-ground traversability estimation for off-road environments. arXiv preprint arXiv:2309.08814 .
- Narayanan A, Siravuru A and Dariush B (2020) Gated recurrent fusion to learn driving behavior from temporal multimodal data. IEEE Robotics and Automation Letters 5(2): 1287–1294.
- Polack P, Altché F, d'Andréa Novel B and de La Fortelle A (2018) Guaranteeing consistency in a motion planning and control architecture using a kinematic bicycle model. In: 2018 Annual American Control Conference (ACC). IEEE, pp. 3981–3987.
- Ramirez-Robles E, Starostenko O and Alarcon-Aquino V (2024) Real-time path planning for autonomous vehicle off-road driving. PeerJ Computer Science 10: e2209.
- Reina G and Messina A (2019) Vehicle dynamics estimation via augmented extended kalman filtering. Measurement 133: 383–395.
- Ronneberger O, Fischer P and Brox T (2015) U-net: Convolutional networks for biomedical image segmentation. In: Medical image computing and computer-assisted intervention–MICCAI 2015: 18th international conference, Munich, Germany, October 5-9, 2015, proceedings, part III 18. Springer, pp. 234–241.
- Saemundsson S, Terenin A, Hofmann K and Deisenroth M (2020) Variational integrator networks for physically structured embeddings. In: International Conference on Artificial Intelligence and Statistics. PMLR, pp. 3078–3087.
- Schwarz M, Rodehutsors T, Droschel D, Beul M, Schreiber M, Araslanov N, Ivanov I, Lenz C, Razlaw J, Schüller S, Schwarz D, Topalidou-Kyniazopoulou A and Behnke S (2017) Nimbro rescue: solving disaster-response tasks with the mobile manipulation robot momaro. Journal of Field Robotics 34(2): 400–425.
- Serban R, Olsen N, Negrut D, Recuero A and Jayakumar P (2017) A co-simulation framework for high-performance, high-fidelity simulation of ground vehicle-terrain interaction. In: Conference: NATO AVT-265 Specialists' Meeting, Vilnius, Lithuania (May 2017), volume 23. p. 24.
- Su S, Hao C, Weaver C, Tang C, Zhan W and Tomizuka M (2023) Double-iterative gaussian process regression for modeling error compensation in autonomous racing. IFAC-PapersOnLine 56(2): 7940–7947.
- Taheri S, Sandu C, Taheri S, Pinto E and Gorsich D (2015) A technical survey on terramechanics models for tire-terrain interaction used in modeling and simulation of wheeled vehicles. Journal of Terramechanics 57: 1–22.
- Tanelli M, Ferrara A and Giani P (2012) Combined vehicle velocity and tire-road friction estimation via sliding mode observers. In:

- 2012 IEEE International Conference on Control Applications. IEEE, pp. 130–135.
- Tremblay JF, Manderson T, Noca A, Dudek G and Meger D (2021) Multimodal dynamics modeling for off-road autonomous vehicles. In: 2021 IEEE International Conference on Robotics and Automation (ICRA). IEEE, pp. 1796–1802.
- Triest S, Sivaprakasam M, Wang SJ, Wang W, Johnson AM and Scherer S (2022) Tartandrive: A large-scale dataset for learning off-road dynamics models. In: 2022 International Conference on Robotics and Automation (ICRA). IEEE, pp. 2546–2552.
- Vosahlik D, Cech J, Hanis T, Konopisky A, Rurtle T, Svancar J and Twardzik T (2021) Self-supervised learning of camera-based drivable surface friction. In: 2021 IEEE International Intelligent Transportation Systems Conference (ITSC). IEEE, pp. 2773–2780.
- Vulpi F, Milella A, Marani R and Reina G (2021) Recurrent and convolutional neural networks for deep terrain classification by autonomous robots. Journal of Terramechanics 96: 119–131.
- Wang C, Gao D, Xu K, Geng J, Hu Y, Qiu Y, Li B, Yang F, Moon B, Pandey A, Aryan, Xu J, Wu T, He H, Huang D, Ren Z, Zhao S, Fu T, Reddy P, Lin X, Wang W, Shi J, Talak R, Cao K, Du Y, Wang H, Yu H, Wang S, Chen S, Kashyap A, Bandaru R, Dantu K, Wu J, Xie L, Carlone L, Hutter M and Scherer S (2023a) PyPose: A library for robot learning with physics-based optimization. In: IEEE/CVF Conference on Computer Vision and Pattern Recognition (CVPR). URL <https://arxiv.org/abs/2209.15428>.
- Wang C, Ji K, Geng J, Ren Z, Fu T, Yang F, Guo Y, He H, Chen X, Zhan Z, Du Q, Su S, Li B, Qiu Y, Du Y, Li Q, Yang Y, Lin X and Zhao Z (2024a) Imperative learning: A self-supervised neural-symbolic learning framework for robot autonomy. arXiv preprint arXiv:2406.16087 URL <https://arxiv.org/abs/2406.16087>.
- Wang R, Fu M, Yu J, Yang Y and Song W (2024b) Risk-inspired aerial active exploration for enhancing autonomous driving of ugv in unknown off-road environments. In: 2024 IEEE International Conference on Robotics and Automation (ICRA). IEEE, pp. 14390–14396.
- Wang SJ, Zhu H and Johnson AM (2024c) Pay attention to how you drive: Safe and adaptive model-based reinforcement learning for off-road driving. In: 2024 IEEE International Conference on Robotics and Automation (ICRA). IEEE, pp. 16954–16960.
- Wang Y, Wang J, Jiang J, Xu S and Wang J (2023b) Sa-lstm: A trajectory prediction model for complex off-road multi-agent systems considering situation awareness based on risk field. IEEE Transactions on Vehicular Technology 72(11): 14016–14027.
- Wang Y, Wang J, Yang Y, Li Z and Zhao X (2022) An end-to-end deep reinforcement learning model based on proximal policy optimization algorithm for autonomous driving of off-road vehicle. In: International Conference on Autonomous Unmanned Systems. Springer, pp. 2692–2704.
- Wasfy TM, Jayakumar P, Mechergui D and Sanikommu S (2018) Prediction of vehicle mobility on large-scale soft-soil terrain maps using physics-based simulation. International Journal of Vehicle Performance 4(4): 347–381.
- Wellhausen L, Dosovitskiy A, Ranftl R, Walas K, Cadena C and Hutter M (2019) Where should i walk? predicting terrain properties from images via self-supervised learning. IEEE Robotics and Automation Letters 4(2): 1509–1516.
- Wu J (2024) Physical scene understanding. AI Magazine 45(1): 156–164.
- Wu J, Luo Z, Zhang N and Zhang Y (2015) A new uncertain analysis method and its application in vehicle dynamics. Mechanical Systems and Signal Processing 50: 659–675.
- Xiao W, Xue H, Tao T, Kalaria D, Dolan JM and Shi G (2024) Anycar to anywhere: Learning universal dynamics model for agile and adaptive mobility. arXiv preprint arXiv:2409.15783.
- Zhang Z, He W, Wu F, Quesada L and Xiang L (2024) Development of a bionic hexapod robot with adaptive gait and clearance for enhanced agricultural field scouting. Frontiers in Robotics and AI 11: 1426269.
- Zhao S, Zhang H, Wang P, Nogueira L and Scherer S (2021) Super odometry: Imu-centric lidar-visual-inertial estimator for challenging environments. In: 2021 IEEE/RSJ International Conference on Intelligent Robots and Systems (IROS). IEEE, pp. 8729–8736.
- Zhao Z, Li B, Du Y, Fu T and Wang C (2024) Physord: A neuro-symbolic approach for physics-infused motion prediction in off-road driving. arXiv preprint arXiv:2404.01596.
- Zhu JJ, Khajepour A, Spike J, Chen SK and Moshchuk N (2016) An integrated vehicle velocity and tyre-road friction estimation based on a half-car model. International Journal of Vehicle Autonomous Systems 13(2): 114–139.